



**1 JUICE-MAJIS Earth observations during the 2024 gravity assist: first analysis  
2 and comparison with PRISMA data**

3

4 Fabrizio Oliva<sup>1,\*</sup>, Emiliano D'Aversa<sup>1</sup>, Alessandra Migliorini<sup>1</sup>, Giuseppe Piccioni<sup>1</sup>, François Poulet<sup>2</sup>,  
5 Yves Langevin<sup>2</sup>, Gianrico Filacchione<sup>1</sup>, Mauro Ciarniello<sup>1</sup>, Sébastien Rodriguez<sup>2</sup>, Benoît Seignovert<sup>2</sup>,  
6 Alessandro Mura<sup>1</sup>, Leigh N. Fletcher<sup>4</sup>, Angelo Zinzi<sup>3</sup>, Marco Giardino<sup>3</sup>, Ettore Lopinto<sup>3</sup>, Giuseppe  
7 Sindoni<sup>3</sup>, Christina Plainaki<sup>3</sup>

8 \*Correspondence: [fabrizio.oliva@inaf.it](mailto:fabrizio.oliva@inaf.it)

9

10 <sup>1</sup>*Istituto di Astrofisica e Planetologia Spaziali (IAPS/INAF), Rome, Italy;*

11 <sup>2</sup>*Institut d'Astrophysique Spatiale, CNRS/Université Paris-Saclay, 91405 Orsay Cedex, France.*

12 <sup>3</sup>*Agenzia Spaziale Italiana (ASI), Rome, Italy.*

13 <sup>4</sup>*School of Physics and Astronomy, University of Leicester, University Road, Leicester, LE1 7RH, UK.*

14

15 **Abstract**

16

17 The *JUupiter ICy moons Explorer* spacecraft (JUICE) performed a Lunar-Earth gravity assist  
18 maneuver on 20th August 2024, during which the scientific instruments were turned on to  
19 test their functionality. At the Earth, the *Moon and Jupiter Imaging Spectrometer* (MAJIS)  
20 acquired a sequence of multispectral images over the Western Pacific Ocean at tropical  
21 latitudes. In parallel, an observing campaign was also conducted by the Earth-orbiting  
22 PRISMA imaging spectrometer, with the purpose of validating MAJIS spectral observations  
23 with independent measurements of the same kind.

24 These two datasets are here exploited to investigate and compare several atmospheric and  
25 cloud properties, including composition, temperatures, and atmospheric gravity waves. In the  
26 MAJIS spectral range, covering the 500-5560 nm wavelengths, we identified major and  
27 minor atmospheric gases, including O<sub>2</sub>, H<sub>2</sub>O, CO<sub>2</sub>, O<sub>3</sub>, CH<sub>4</sub>, N<sub>2</sub>O. Since MAJIS observations  
28 mostly covered diffuse cloudiness over the ocean, our analysis mainly focused on the  
29 discrimination of clouds' properties and altitudes. We verified that ice particles are  
30 widespread in the data, allowing for an investigation of their properties (e.g. crystallinity)  
31 through different spectral signatures. The only land features identified in MAJIS data are not  
32 observed in daylight, hence only a thermal emission analysis is presented. Finally, the  
33 coverage of the 4300 nm CO<sub>2</sub> band enables the identification of high altitude structures,  
34 revealing the presence of several atmospheric wave packets, likely induced by convective  
35 events, or lightning strikes known to have occurred at the time of the flyby. The present  
36 analysis demonstrates how MAJIS data can contribute to the scientific investigation of an  
37 atmospheric environment, and provide the first benchmark in the analysis of water ice,  
38 whose characterization in the Jovian system will be of primary importance for the JUICE  
39 mission.

40

41 **1. Introduction**

42

43 On the 20th of August 2024 the JUICE spacecraft performed a first *Lunar-Earth Gravity*  
44 *Assist* (LEGA). In this study we will focus on the *Earth Gravity Assist* (EGA) alone, during  
45 which the *Moons and Jupiter Imaging Spectrometer* (MAJIS, Poulet et al., 2024a) was turned  
46 on, providing its very first observations of a planetary target. A general overview of the flyby  
47 is given in Poulet et al. (this issue) while valuable information about MAJIS operations,



48 functioning and performances is given in Langevin et al. and Seignovert et al. (this issue).  
49 Different Earth observing spectrometers were coordinated to provide spatially and temporally  
50 comparable observations (Poulet et al., this issue). Among these, we exploit PRISMA  
51 spectrometer data as a proxy to compare with MAJIS observations, even if the different  
52 times and regions of acquisition prevent a direct comparison of the scans (see Section 2).

53 JUICE flew over Western Pacific Ocean at tropical latitudes, moving approximately from  
54 Sumatra to Hawaii islands and spanning local times from about 03:00 to 10:30 (see Table  
55 1). The majority of these measurements took place over the ocean, allowing a broad  
56 characterization of atmospheric gaseous composition and structure (Section 2.3.2). Land  
57 features are only marginally detected in a couple of observations mainly in the thermal range  
58 (Section 4.4).

59 Given the widespread presence of clouds and the early local times of acquisition (Section 2),  
60 ice is observed in almost all MAJIS scans (Section 4.1), allowing benchmarking of the  
61 spectrometer's response to this observable in view of Jupiter's icy satellites investigation.  
62 Also atmospheric waves, whose role is fundamental in regulating the middle-atmosphere  
63 circulation (e.g. Hamilton, 1996; Fritts and Alexander, 2003), are detected in many MAJIS  
64 observations. Given their link with orography (Queney 1948; Kim et al. 2003) or with the  
65 occurrence of thunderstorms (Taylor and Hapgood, 1988; Dewan et al. 1998) we investigate  
66 their dependence with strong convective events or lightning strikes (Section 4.4).

67 The manuscript is arranged in sections describing the data (Section 2), the methods for their  
68 investigation (Section 3) and the obtained results (Section 4). Such a wide ensemble of  
69 atmospheric observable features is finally discussed in the context of Jupiter science in  
70 Section 5.

71

## 72 2. Observations

73

### 74 2.1. MAJIS EGA Data

75

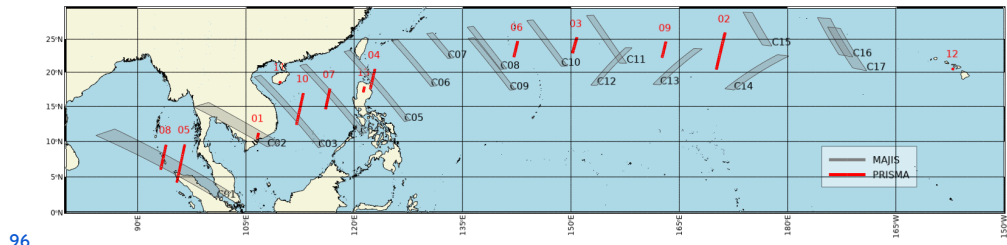
76 MAJIS is a dispersion grating imaging spectrometer operating between 500 and 5560 nm by  
77 means of two spectral channels (Poulet et al., 2024a). The first channel (VISNIR, 500–2350  
78 nm) is characterized by nominal spectral resolution and sampling of 2.9–4.6 nm and 3.5–3.8  
79 nm/band respectively, while the second (IR, 2270–5560 nm) works with a spectral resolution  
80 of 5.5–7.0 nm and a sampling of 5.9–6.9 nm/band. The nominal instrument's instantaneous  
81 field of view (IFOV) is 150  $\mu$ rad/pixel. MAJIS concept has been optimized for the  
82 characterization of the surface and near-surface environment of Jupiter's icy moons (Poulet  
83 et al., 2024a), as well as for the investigation of Jupiter's atmosphere (Fletcher et al., 2023).  
84 Detailed descriptions of the instrument functioning, operations and calibration are given in  
85 Haffoud et al. (2024), Langevin et al. (2024), Poulet et al. (2024b), Filacchione et al. (2024),  
86 Rodriguez et al. (2024), Vincendon et al. (2024), and Stefani et al. (2025). Scene geometry is  
87 reconstructed via the SPICE-NAIF toolkit (Acton, 1996; Acton et al., 2018) and kernels  
88 provided by ESA ("JUICE SPICE Kernel Dataset," 2019).

89 Figure 1 and Table 1 summarize footprint locations and main basic properties of the 17  
90 MAJIS EGA data investigated in this work (see Poulet et al., this issue, for further  
91 instrumental parameters). Two additional cubes, targeted off-limb for calibration purposes  
92 (Poulet et al., this issue), are not considered here. Each MAJIS acquisition consists of



93 hyperspectral *cubes* (i.e. 2D spatial frames with a third spectral dimension) collected as  
 94 pushbroom spectral scans via internal mirror rotation, with different widths and lengths.

95



96

97 **Figure 1:** Geographical coverage of the investigated observations, MAJIS in grey color,  
 98 PRISMA in red color (coastlines data from OpenStreetMap, available under the Open  
 99 Database License).

100

101 The first 4 cubes (C1 to C4) pointed to the Earth surface at nighttime and contain a  
 102 significant signal only in the thermal part of the spectrum ( $\lambda > 3000$  nm). The only exception  
 103 is C1, where a lightning emission is identifiable at visible wavelengths (D'Aversa et al., this  
 104 issue). C5 is straddling the terminator and is the first cube containing information on the  
 105 dayside ocean and clouds. Some coastlines are identifiable in C4 and C5 at thermal  
 106 wavelengths, as it will be discussed in Section 4.4. All the subsequent cubes (C6 to C17) are  
 107 acquired in daylight and hence the full spectrum can be investigated, even if they only cover  
 108 the ocean surface mostly under cloudy/stormy conditions.

109 Cubes from C11 on have been acquired with longer integration times, with the purpose of  
 110 testing the instrument response. This leads to signal saturation in many regions (especially  
 111 at visual wavelengths over clouds, see Section 2.3.1), that have been removed from our  
 112 analysis. The spatial resolution in this dataset is quite stable (about 1.4 km per pixel, slightly  
 113 affected by motion smearing) and is suited for the investigation of both homogeneous and  
 114 localized cloud structures. On the other hand, the IFOV is affected by unresolved cloudiness  
 115 (likely widespread) which dilutes the low reflectivity of deep water hence preventing the  
 116 acquisition of clear-sky ocean (Section 2.3.1, Figure 2).

117

118 **Table 1:** MAJIS observing parameters during EGA. Phase angle is always close to 90°.

	ID	target	incidence angle (°)	emission angle (°)	local time (h)	instantaneous resolution (km/px)
C1	20240820212509	surface night	115-130	28-42	03:00 – 04:18	1.80
C2	20240820212818	surface night	106-116	17-27	03:54 – 04:48	1.55
C3	20240820213029	surface night	100-106	12-19	04:30 – 05:12	1.50
C4	20240820213208	surface night	93-100	6-13	05:00 – 05:36	1.45
C5	20240820213347	surface terminator	87-93	0-11	05:24 – 06:00	1.40
C6	20240820213530	surface day	82-87	6-11	05:54 – 06:18	1.35
C7	20240820213644	surface day	79-82	11-14	06:12 – 06:30	1.30



C8	20240820213731	surface day	72-77	17-20	06:36 – 07:00	1.30
C9	20240820213840	surface day	71-76	14-20	06:36 – 07:06	1.30
C10	20240820214003	surface day	64-69	24-27	07:12 – 07:36	1.30
C11	20240820214117	surface day	56-61	32-37	07:48 – 08:12	1.30
C12	20240820214231	surface day	55-60	29-34	07:48 – 08:12	1.25
C13	20240820214350	surface day	46-52	39-45	08:24 – 08:54	1.30
C14	20240820214509	surface day	34-42	50-58	09:06 – 09:42	1.35
C15	20240820214628	surface day	36-41	49-53	09:18 – 09:36	1.30
C16	20240820214720	surface day	26-32	60-65	10:00 – 10:18	1.40
C17	20240820214813	surface day	23-31	60-66	10:06 – 10:30	1.40

119

120 **2.2. PRISMA data**

121

122 An observing campaign coordinated to the EGA was conducted by the mission PRISMA  
123 (PRRcursoro IperSpettrale della Missione Applicativa), managed by the Italian Space  
124 Agency. The mission hosts a visible and near-infrared imaging spectrometer, covering a  
125 range (400-2500 nm) compatible with the MAJIS-VISNIR channel but having a coarser  
126 spectral resolution (~12 nm) in turn compensated by a higher spatial resolution (~30  
127 m/pixel). Details about the instrument and the mission can be found in Pignatti et al. (2013),  
128 while mission characteristics, access, products, calibration, geometry navigation and data  
129 policy are fully described in Lopinto et al. (2021).

130 PRISMA sequences (13 in total, red rectangles in Figure 1, main parameters summarized in  
131 Table 2) consist of a variable number of 30 x 30 km hyperspectral cubes, each composed of  
132 1000 x 1000 spatial pixels. Due to the PRISMA orbit (Sun-Synchronous-Low-Earth-Orbit),  
133 observations are acquired at a fixed solar local time (~10:30), making it impossible to  
134 achieve spatial/temporal coincidence with MAJIS ones (see next section).

135

136 Table 2: PRISMA observations acquired in coordination with JUICE.

PRISMA sequence	Num cubes	Start UTC	Solar zenith angle (°)	Emission angle (°)	Cloud coverage (%)	Δt (PRISMA-MAJIS) (h)
01	3	2024-08-17 03:34	20.3	14.6	14	-90.9
02	21	2024-08-18 23:13	23.4	17.1	8	-46.45
03	9	2024-08-19 00:50	20.6	20.7	9	-44.83
04	11	2024-08-19 02:22	21.4	4.2	100	-43.19
05	21	2024-08-19 04:08	22.7	1.2	73	-41.52
06	9	2024-08-20 01:07	23.6	16.6	2	-20.55
07	11	2024-08-20 02:46	22.5	18.4	18	-18.90



08	13	2024-08-20 04:25	21.0	16.0	98	-17.24
09	9	2024-08-20 23:46	23.2	12.3	1	2.11
10	17	2024-08-21 03:03	22.0	12.0	5	5.39
11	3	2024-08-22 03:19	21.7	5.6	20	29.66
12	1	2024-08-22 21:07	22.2	7.6	16	47.45
13	3	2024-08-25 02:32	21.6	4.3	7	100.88

137

### 138 2.3. General comparison overview

139

140 Both MAJIS and PRISMA acquired multispectral data covering the same kinds of structures,  
141 offering a useful benchmark for checking MAJIS capabilities in detecting and analyzing  
142 specific features of scientific interest. In the following section we investigate how the spectral  
143 signatures of the main atmospheric gases and of clouds are affected by the different  
144 spatial/spectral resolutions and observing conditions. When reflectances are discussed,  
145 they are obtained for both instruments by converting radiances using the Kurucz solar  
146 spectrum ("newkur") available in the MODTRAN radiative transfer package (Berk et al.,  
147 2014).

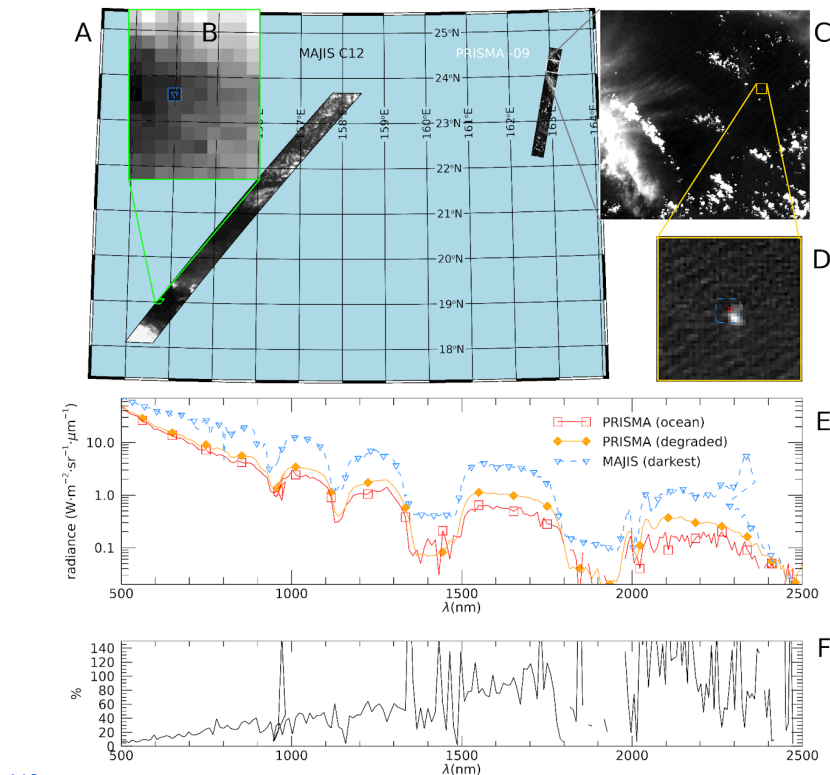
148

#### 149 2.3.1. Ocean/clouds spectra first comparison

150

151 Figure 2 shows the two closest PRISMA and MAJIS cubes (~550 km and ~2 h apart),  
152 covering open ocean areas overlaid by a different amount of clouds. In this framework, the  
153 most robust spectral radiance comparison should consider ocean cloud-free spectra,  
154 expected to be quite stable in space and time and very dark at visual wavelengths (given the  
155 very low ocean albedo, ~4%). However, the comparison between the two instruments  
156 (Figure 2E) highlights that the darkest MAJIS signals are still brighter than those from  
157 PRISMA, possibly suggesting enhanced cloud/aerosol content. Indeed, the higher spatial  
158 resolution of PRISMA data reveals a number of small-scale structures, likely unresolved by  
159 MAJIS, yet affecting its signal. For instance, the small bright feature imaged by PRISMA in  
160 Figure 2D, covering only a portion of a MAJIS pixel footprint, may induce spectral variations  
161 of the ocean spectrum up to 50% (Figure 2F) once observed at the MAJIS resolution scale.

162



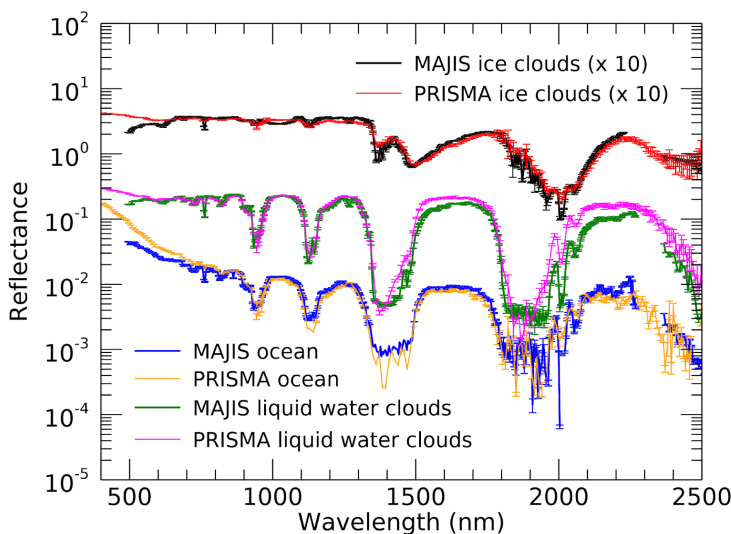
163  
 164 **Figure 2: A)** MAJIS observation C12 and PRISMA sequence P09 (~2h apart) shown at 875  
 165 nm in an equal-area projection. **B)** Blow-up of the darkest area in the MAJIS image,  
 166 highlighting individual pixels' size. **C)** The second cube of the PRISMA sequence is shown in  
 167 its full extension of 1000x1000 pixels. **D)** Blow-up of an area of PRISMA data encompassing  
 168 a small bright cloud. The blue dashed box shows the approximate size of a MAJIS pixel. **E)**  
 169 Single-pixel spectra from the darkest pixels of MAJIS (blue color, triangle symbol in B) and  
 170 PRISMA (red curve, red square in D). The orange curve represents a PRISMA spectrum  
 171 degraded to MAJIS resolution (average inside the blue box of panel D). The MAJIS spectrum  
 172 is multiplied by the ratio of solar incidence cosines (=1.82) to achieve a radiance level  
 173 comparable with PRISMA. **F)** Effect of spectral degradation in PRISMA data, shown as the  
 174 relative difference between the red and orange curves of panel E.

175  
 176 Most of the spectral variability in both datasets is driven by changes in the H<sub>2</sub>O absorption  
 177 bands. Besides the general low reflectivity, ocean spectra are characterized by the presence  
 178 of large and often saturated water absorption bands. On the other hand, H<sub>2</sub>O clouds (either  
 179 composed of liquid droplets, ice crystals or a mixture) can easily be identified through RGB  
 180 imaging from both datasets due to their bright appearance (Section 3.1). H<sub>2</sub>O bands are less  
 181 saturated over clouds, where light scattering prevents photons from reaching the  
 182 underneath, more absorbing, atmospheric layers. Ice clouds' discrimination is basically  
 183 driven by the spectral shift of absorption bands between solid and liquid H<sub>2</sub>O phase (Section  
 184 3.1). The comparison of spectral signatures related to the ocean and clouds (main spectral

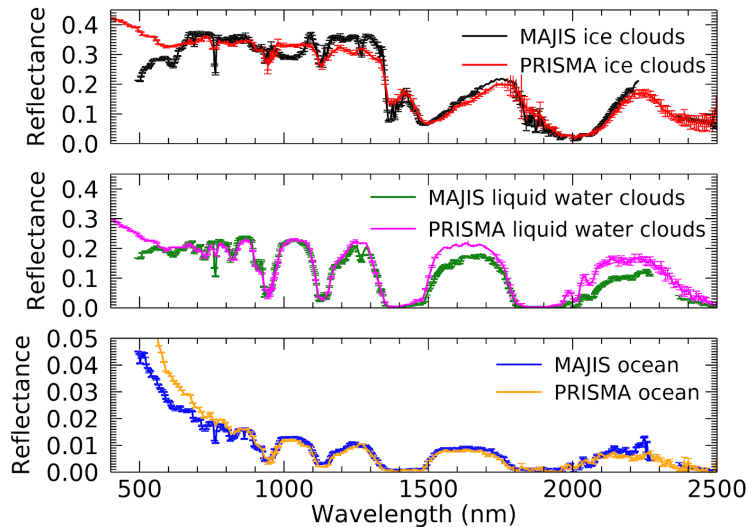


185 endmembers for both instruments) is shown in Figure 3A-B in log and linear scale  
186 respectively (refer to Figures 4 and 5 for the gaseous features identification). This should be  
187 considered as qualitative, since spectra acquired at different locations, geometries and local  
188 times are considered (see Tables 1 and 2). Therefore, clouds are likely characterized by  
189 different vertical distributions and microphysical properties, driven by a radiative forcing that  
190 is changing between early and mid-morning. Also, differential sun-glint effects (dependent on  
191 geometry and wind strength) could produce differences in the overall reflectivity of the  
192 ocean. All these effects are likely to contribute to non-linear offsets in the continuum below  
193 about 700 nm (straylight could also have an impact here), and slightly different depth and  
194 shape of water absorption bands, not ascribable solely to differences in spectral resolution.

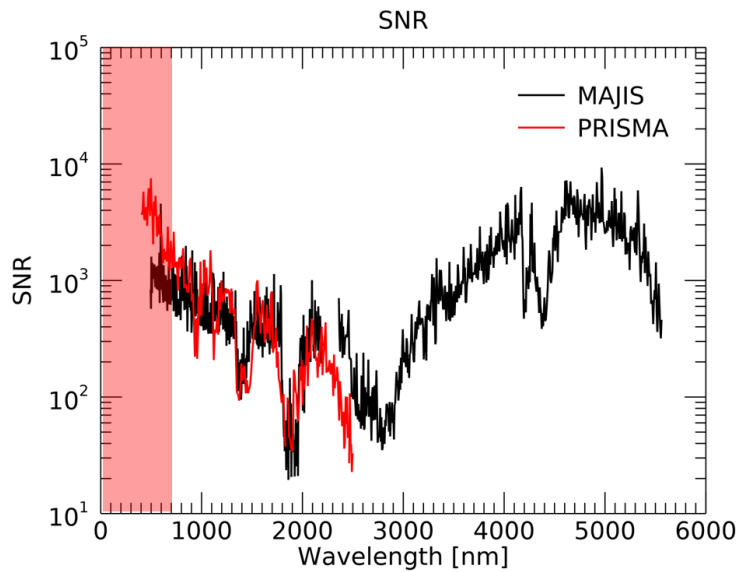
195



196 A



197 B



198 C

199 **Figure 3:** comparison between MAJIS and PRISMA reflectances in log (A) and linear (B)  
 200 scales related to ocean, liquid water clouds and ice water clouds (the latter multiplied by 10  
 201 for clarity in panel A). PRISMA spectra are selected from two orbits in session 7, MAJIS  
 202 ones from orbits C7 (ice clouds) and C10 (ocean and liquid water clouds). Panel C shows  
 203 the SNR estimated for the two instruments (cube C15 for MAJIS, one cube of session 07 for  
 204 PRISMA) as described in Section 2.3.1. The red shaded area indicates the spectral region  
 205 possibly affected by straylight contamination, not yet fully assessed in both datasets.

206



207 The three endmembers in Figure 3 show similar trends in reflectivity, with the main  
208 absorption bands' shape correctly reproduced, even if the probed atmospheric structure is  
209 probably not the same. For example, MAJIS liquid water clouds spectrum shows wider wings  
210 and a flatter bottom for the bands at 1400 and 1900 nm, suggesting different scattering  
211 properties in the atmospheric column for the two cases (see Section 4.2.4). A slightly flatter  
212 bands' bottom is also observed in the ocean spectrum (blue compared to the orange  
213 PRISMA spectrum). On one side, this could indicate that early-morning thin clouds in the  
214 mid-high troposphere are mixed in MAJIS footprint, preventing the formation of the narrower  
215 water lines inside the bands (MAJIS spectrum refers to 7:30 local time, when the presence of  
216 unresolved hazes is likely). On the other hand, such low signals could reach the instrument  
217 noise equivalent spectral radiance (NESR), hence explaining the featureless bands' bottom.  
218 We derived an upper limit for the NESR by investigating the darkest ocean region in the  
219 selected MAJIS cube (C10), resulting in about  $10^{-3}$   $\text{W}/(\text{m}^2 \mu\text{m} \text{sr})$  at 1900 nm. This value  
220 corresponds to reflectances of  $10^{-4}$ , about one order of magnitude below the ocean signal at  
221 that wavelength (Figure 3A), hence making the mixed-footprint hypothesis more likely. The  
222 occurrence of saturation in some parts of MAJIS spectrum is highlighted in the ice clouds  
223 comparison, evident as a broad absorption between 900 and 1100 nm in Figure 3B. MAJIS  
224 uncertainties are extensively discussed in the paper by Poulet et al. (this issue), but here we  
225 attempt an *a posteriori* estimation of the spectral signal to noise ratios (SNR) for both  
226 instruments by performing a statistical analysis of spatial fluctuations computed in 5x5 pixels  
227 boxes (Figure 3C). For each wavelength (excluding saturated regions) we select those  
228 regions producing the minimum relative error, hence representing both noise statistics and  
229 true variations in the observed scene. As a result, the spectral SNRs in Figure 3C refer to  
230 wavelength-dependent locations in the respective cubes, rather than to a single region. This  
231 means that the high frequency oscillations in the red and black lines are mostly driven by  
232 spatial differences between the selected boxes (at the scale covered by the respective  
233 cubes). Values below  $\sim 700$  nm (red shaded area in Figure 3C) are possibly contaminated by  
234 the presence of straylight affecting the actual trend of the SNR for both instruments.

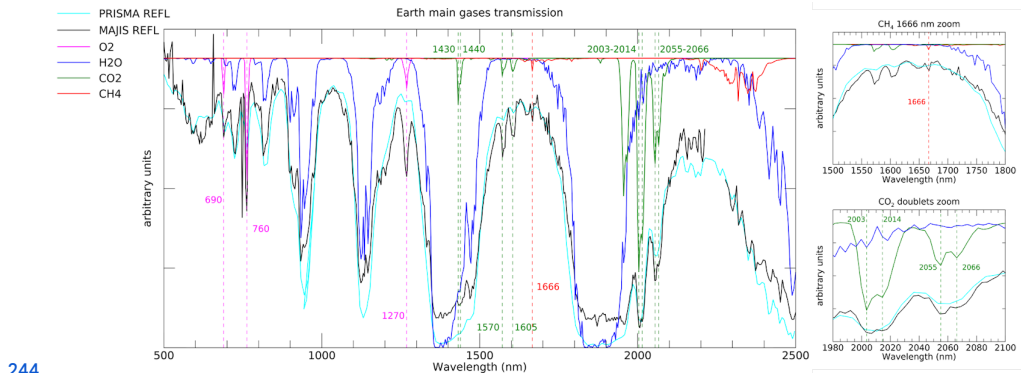
235

### 236 2.3.2. Gaseous compounds

237

238

239 Figure 4 compares sample MAJIS/PRISMA reflectance spectra with two-way vertical  
240 transmission due to  $\text{O}_2$ ,  $\text{H}_2\text{O}$ ,  $\text{CO}_2$ ,  $\text{CH}_4$ ,  $\text{N}_2\text{O}$  and  $\text{CO}$ , based on an average vertical structure  
241 from Efremenko and Kokhnovsky (2021), calculated through line-by-line method with line  
242 parameters from the HITRAN database (Gordon et al., 2022), and then convolved at the  
243 MAJIS spectral resolution.



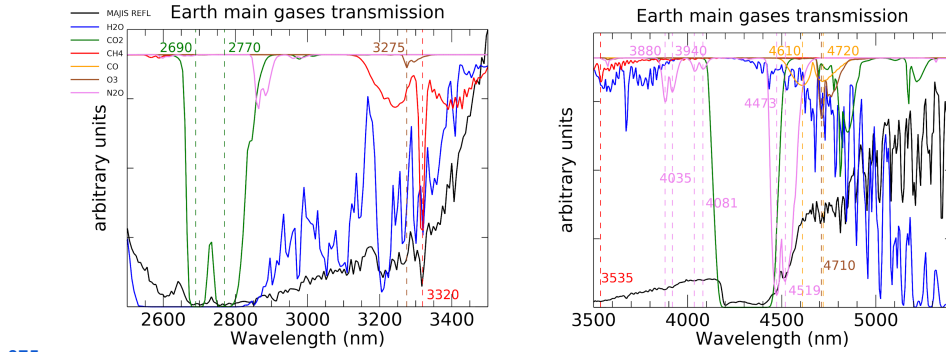
244

245 Figure 4: MAJIS (black, taken from C7) and PRISMA (cyan, taken from session 7)  
246 normalized reflectances (both pertaining to liquid water cloud scenarios) compared to main  
247 Earth's atmospheric gases two-way transmissions convolved on MAJIS spectral grid. Vertical  
248 dashed lines indicate the main non-H<sub>2</sub>O molecular lines identifiable in the observations.  
249 Zooms related to the CH<sub>4</sub> 1666 nm absorption line, and the CO<sub>2</sub> doublets at 2003-2014 nm /  
250 2055-2066 nm are shown in the upper and lower right panels respectively.

251

252 In their common spectral range, both instruments allow to identify the main absorption  
253 features of H<sub>2</sub>O, O<sub>2</sub> and CO<sub>2</sub> (Figure 4, see also Poulet et al., this issue). The reduced  
254 spectral resolution of PRISMA makes it difficult to resolve narrow features like the methane  
255 absorption at 1666 nm (Figure 4, upper right panel), the close doublets of CO<sub>2</sub> at 2003-2014  
256 nm and 2055-2066 nm (Figure 4, lower right panel), or shallower lines of water. On the other  
257 hand, the PRISMA spatial resolution is expected to reduce the spatial mixing of different  
258 types of surfaces or aerosols, allowing a more robust tracking of localized and transient  
259 phenomena (e.g. smog layers, ice patches, oil spills, CO<sub>2</sub> emissions, etc.). At wavelengths  
260 around 600 nm a broad absorption possibly matching the O<sub>3</sub> Chappuis band appears in both  
261 datasets. In MAJIS, this is enhanced over thick clouds and in particular in grazing  
262 illumination conditions (Section 4.4) in which the atmospheric column above ~20 km is  
263 directly illuminated resulting in a very long photon path length that increases the absorption  
264 from O<sub>3</sub> in the scattered light (most of terrestrial ozone resides between altitudes of 20 and  
265 40 km). Nevertheless, a better quantification requires a more rigorous assessment of the  
266 straylight contamination (Langevin et al., this issue).

267 Besides the better spectral resolution, MAJIS also has the advantage of an extended  
268 spectral range covering wavelengths from 2500 nm up to 5560 nm. In this range, thermal  
269 emission dominates and provides information on the temperature of the sampled  
270 atmospheric layers, or of the ocean and clouds. This interval is characterized by several H<sub>2</sub>O  
271 absorption bands (the stronger one centered at about 2700 nm), strong and saturated CO<sub>2</sub>  
272 ones at 2690, 2770 and 4300 nm, and weaker CH<sub>4</sub>, O<sub>3</sub>, CO and N<sub>2</sub>O signatures (Figure 5).  
273 In particular, the strong CO<sub>2</sub> absorption (and emission) at 4300 nm, can be exploited for the  
274 estimation of the vertical structure of atmospheric temperatures (see Poulet et al., this issue).



275

276 **Figure 5:** MAJIS (black) reflectance compared to main Earth's atmospheric gases  
277 two-way transmissions in the 2500 - 3500 nm range (left) and 3500-5400 nm range (right).  
278 Thermal emission is not considered in the transmission computation and all spectra are  
279 convolved to the MAJIS spectral grid.

280

### 281 3. Methods

282

283 In this section we describe different methods for investigating the information content in the  
284 data, including surface/cloud features identification (Section 3.1), ice characterization  
285 (Section 3.2), clouds' altitude estimation (Section 3.3) and high-altitude features investigation  
286 (Section 3.4).

287

#### 288 3.1. Surface and clouds identification

289

290 In principle, Earth observations can encompass different types of surfaces, commonly  
291 discriminated spectrally through indices expressed in the formalism of *Normalized Difference*  
292 *spectral Indices* (NDIs, see Wolf, 2010 for a general review). Useful examples are given in  
293 Hurley et al., 2014 (dealing with Rosetta/VIRTIS-M data, Coradini et al., 1999) and in Oliva  
294 et al., 2017 (dealing with both Rosetta and Venus Express/VIRTIS-M data, Drossart et al.,  
295 2004). Table 3 summarizes these indices (derived from spectral endmembers from  
296 Rosetta/VIRTIS-M acquisitions, Figure 6A-B, since MAJIS observations did not cover  
297 surface features in daylight) that we test on PRISMA data (Figure 6C-D) as a benchmark for  
298 the future September 2026 EGA in which Africa observations are planned. A new ocean  
299 index is also defined specifically for MAJIS data, which do not cover all wavelengths of the  
300 nominal ocean NDI. It is worth stressing that the ocean class should not be considered as  
301 representative of clear-sky conditions as it may actually include some amount of aerosol  
302 opacity (Section 2.3.1). No specific index has been adopted for generic clouds identification,  
303 but we rather assign to this class all pixels that do not meet any of the surface classes'  
304 conditions. Indices thresholds can be studied taking advantage of proxy images (e.g. the  
305 PRISMA one shown in Figure 6C, not pertaining to EGA sequence) in which the changing  
306 reflecting structures can be clearly identified. The derived values depend on instrument  
307 features and require specific tuning when switching between different datasets. Figure 6C-D  
308 shows how the different types of spectral classes can be reliably identified, even if, in this  
309 case, no ice clouds are present. Other examples of application of the ocean, clouds and ice  
310 indices from Table 3 to MAJIS and PRISMA data are discussed in Section 4.1. Instead, the



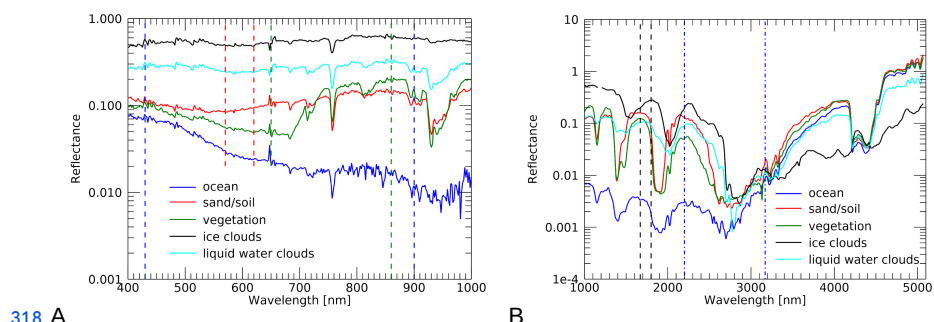
311 application of surface-related indices to MAJIS data did not result in positive identification,  
 312 since land features in MAJIS data are not seen in daylight illumination, making NDIs not  
 313 applicable.

314

SPECTRAL CLASS	SPECTRAL INDEX	SPECTRAL SIGNATURE	FIGURE
Vegetation	NDVI: $\frac{R_{860} - R_{650}}{R_{860} + R_{650}}$	Chlorophyll absorption in the red band	6D
Sand/Soil	NDSI: $\frac{R_{570} - R_{620}}{R_{570} + R_{620}}$	Enhanced contrast between the red and green bands	6D
Ocean	NDWI: $\frac{R_{430} - R_{900}}{R_{430} + R_{900}}$	Enhanced reflectivity in the blue with respect to NIR wavelengths	6D - 12D
MAJIS Ocean	$\frac{R_{2200}}{R_{3170}}$	Low solar reflectivity / large thermal emission	12C
Ice Clouds	$\frac{R_{1670}}{R_{1800}}$	Shift of the 1500 nm H <sub>2</sub> O ice absorption band to longer wavelengths with respect to the liquid phase (different arrangement of hydrogen bonds)	12C - 12D
Cloudy	pixels not assigned to surface types	/	6D - 12C - 12D

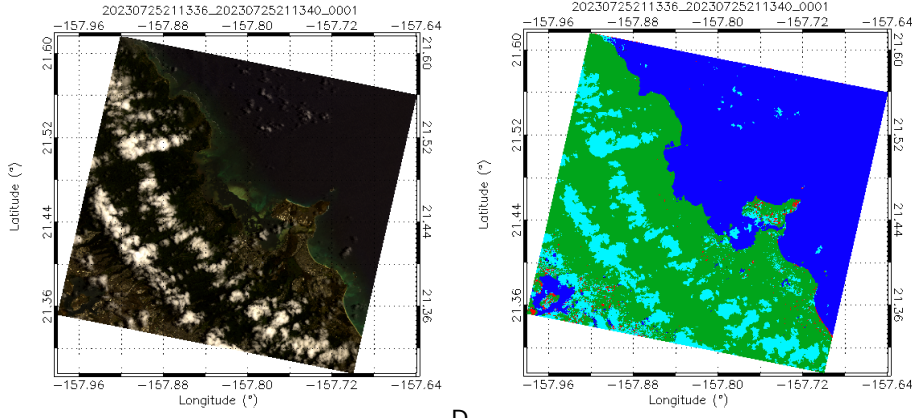
315

316 **Table 3.** Spectral indices for the identification of different spectral classes related to surfaces  
 317 and clouds.



318 A

B



319 C

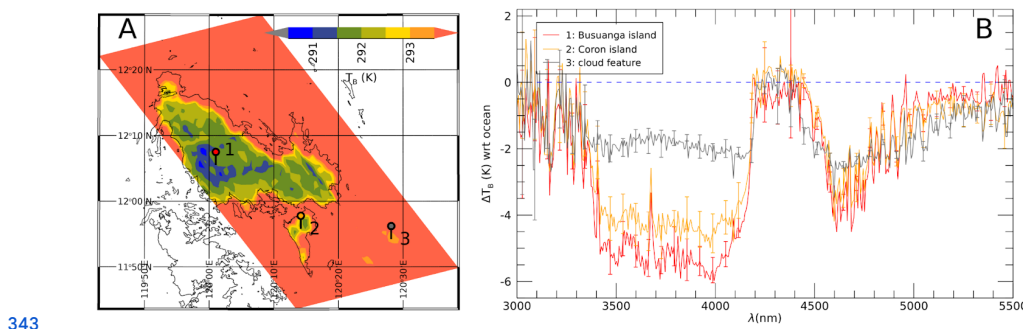
D

320 **Figure 6: A:** Reflectance endmembers of different classes of surface and clouds, derived  
 321 from Rosetta/VIRTIS-M VIS channel Earth observations (Oliva et al., 2017). Vertical dashed  
 322 lines share the color of the corresponding spectral endmember and identify the wavelengths  
 323 adopted in the index definition (blue ones refer to the NDWI). **B:** same as in A but spectra  
 324 are from the NIR channel of VIRTIS-M (blue dashed-dotted lines refer to the MAJIS ocean  
 325 index). **C:** Example of a PRISMA RGB image covering different surface types (data cube  
 326 2023072521336\_20230725213340) targeting the eastern coastal line of Honolulu island  
 327 ( $R=680$  nm;  $G=570$  nm,  $B=440$  nm). **D:** distribution of spectral classes obtained from the  
 328 spectral indices in Table 3. Green pixels indicate vegetation, red ones are sand, cyan ones  
 329 are clouds, blue ones indicate ocean/water (no ice clouds present).

330

331 In the specific conditions of MAJIS EGA sequence, the most robust land identification must  
 332 rely on soil/ocean contrast in thermal emission (Section 4.4), triggered by the different  
 333 thermal inertia of the two classes. However, also the presence of clouds in the line of sight  
 334 induces a decrease of the observed brightness temperature ( $T_B$ ), hence land identification  
 335 requires matching the shapes of low  $T_B$  regions within known coastlines. The largest land  
 336 region emerging in this way is shown in Figure 7 (cube C4), (Philippines's Busuanga and  
 337 Coron islands in cube C4), whose identification also allows a refinement of MAJIS pointing  
 338 reconstruction (Seignovert et al., this issue). The largest brightness temperature contrast for  
 339 both land/ocean and cloud/ocean cases occurs in the 3500-4000 nm and 4600-4800 nm  
 340 spectral ranges, which are less absorbed by atmospheric  $H_2O$  and  $CO_2$ . The application of  
 341 this method to other MAJIS data is illustrated in more detail in Section 4.4.

342



343



344 *Figure 7: Land detection obtained by comparing the shapes of low brightness temperature*  
345 ( $T_B$ ) *regions with known coastlines. A) Identification of Busuanga and Coron islands*  
346 (*markers 1 and 2 respectively*), *colder than the surrounding ocean, as well as clouds (marker*  
347 *3).* **B)** *Spectral contrast in brightness temperature ( $T_B$ ) with respect to the ocean spectrum,*  
348 *measured over the islands (Busuanga in red, Coron in orange) and over a thin cloud (grey*  
349 *curve). Coastlines data from OpenStreetMap, available under the Open Database License.*

350

### 351 3.2. Ice characterization

352

353 MAJIS and PRISMA data allow investigating the distribution of physical properties of ice and  
354 how they relate, for example, to the altitude of the clouds where it is identified (see Sections  
355 4.1 and 4.2). The temperature, crystallinity, grain size, purity, and density affect the shape of  
356 ice absorption bands (in particular the main ones at 1500 nm and 1900 nm) and of the  
357 continuum. Since the long wavelength shoulder of the 2000 nm band encompasses the  
358 noisy junction between the VISNIR and IR channels of MAJIS, we focus on the 1500 nm  
359 band, spectrally well resolved in both MAJIS and PRISMA datasets. This band has a  
360 characteristic asymmetry (due to its differential intensity with respect to the 1900 nm one,  
361 e.g. Stephan et al., 2021) affecting the position and shape of the in-between transmission  
362 window peak (~1700 nm) and has been exploited in the definition of the ice index in Table 3.  
363 Within the 1500 nm band, the weaker 1650 nm absorption is present. Its strength is a proxy  
364 for the degree of the ice crystallinity and temperature (Fink and Larson, 1975; Filacchione et  
365 al., 2016). It is also observable in PRISMA, even if shallower and noisier due to the lower  
366 spectral resolution (see zooms in Figure 8A and B).

367 The 3000 - 4000 nm wavelength range, not accessible to PRISMA, hosts two ice reflection  
368 peaks at around 3100 nm (the Fresnel peak) and 3700 nm (Figure 8C). The former varies in  
369 shape and intensity as a function of the ice crystallinity (Cartwright et al., 2025) while the  
370 latter shifts to longer wavelengths as temperature increases (e.g. Filacchione et al., 2016,  
371 see Section 3.3.3). Fresnel peak position variations are estimated in the data through  
372 cross-correlating each ice spectrum with a constant shape (average peak shape in each  
373 cube) which is rigidly shifted with a 0.1 nm sampling (hence allowing the estimation of the  
374 peak with a sampling better than the nominal MAJIS one). On the other hand, the 3700 nm  
375 peak position is obtained through fitting with a Gaussian function, reliably reproducing its  
376 shape.

377 Another proxy of the ice temperature is the intensity of its thermal emission, becoming  
378 significant at wavelengths larger than 4500 nm (Figure 8D). However, in this range the  
379 emitted radiance is absorbed by a plethora of narrow bands of gaseous water, and therefore  
380 only a narrow transmission window around 4600 nm is suitable for this purpose. Table 4  
381 summarizes these ice spectral features, identifiable in MAJIS and PRISMA data. The  
382 average uncertainties  $\Delta$  are propagated taking into account the SNR estimates described in  
383 Section 2.3.1.

384

385

ICE PARAMETER	$\Delta_{\text{MAJIS}}$	$\Delta_{\text{PRISMA}}$	ICE PROPERTIES
1500 nm band depth	< 1 %	< 1 %	number density / grain size
1500 nm band asymmetry	< 2 %	< 3 %	grain size / crystallinity



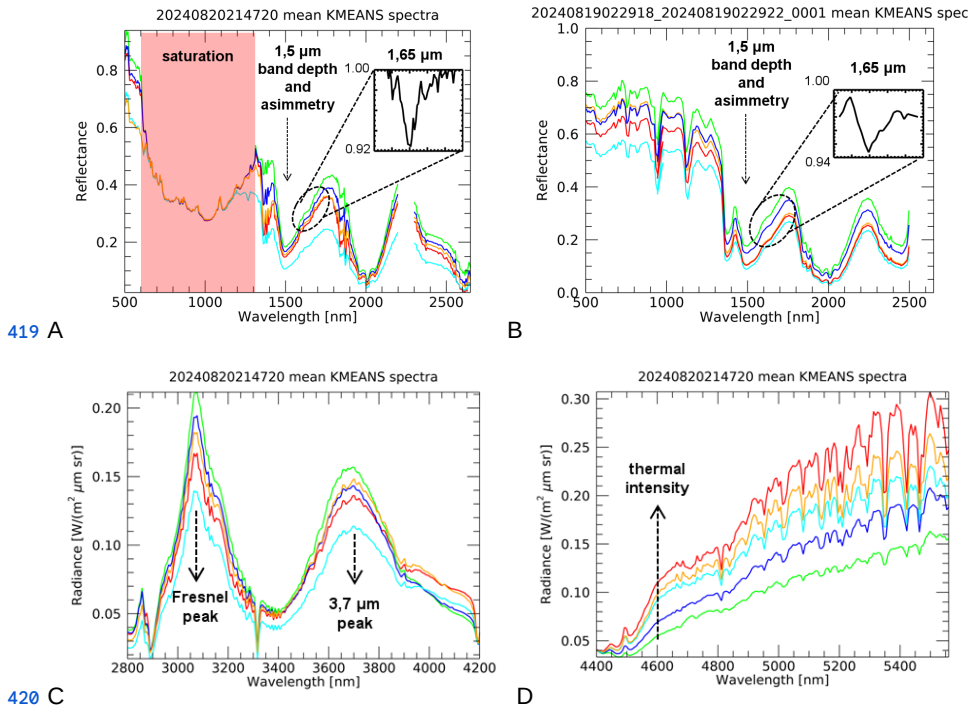
1650 nm band depth	10 %	20 %	crystallinity
<i>Fresnel peak position</i> <i>Fresnel peak intensity</i>	<i>2 nm</i> <i>&lt; 1 %</i>	/	<i>temperature / crystallinity</i>
<i>3700 nm peak position</i> <i>3700 nm peak intensity</i>	<i>0.2 nm</i> <i>&lt; 1 %</i>	/	<i>temperature / crystallinity</i>
<i>4600 nm thermal intensity</i>	<i>&lt; 1 %</i>	/	<i>temperature</i>

386 Table 4: investigated ice parameters and related average uncertainties ( $\Delta$ ) and ice  
387 properties. Entries in italic only refer to MAJIS dataset.

388

389 As a first investigation of the ice spectral variability in MAJIS and PRISMA observations we  
390 exploit the unsupervised K-means classification algorithm included in the ENVI software  
391 package, version 6.0 (Exelis Visual Information Solutions, Boulder, CO, USA,  
392 <https://www.nv5geospatialsoftware.com/Products/ENVI>, accessed on 15 December 2025),  
393 capable of grouping the data through an iterative minimum distance technique (Tou and  
394 Gonzalez, 1974). Given the qualitative approach of this preliminary analysis, we arbitrarily  
395 set the algorithm to produce 5 output clusters for discussing the variability of the main ice  
396 diagnostic spectral features, highlighted in different ranges in Figure 8 for MAJIS cube C16.  
397 These clusters result to be mainly driven by the changing intensity at visible wavelengths,  
398 related to the opacity of the ice clouds. However, it must be noted that since we are also  
399 interested in features pertaining to near infrared wavelengths, in MAJIS case the full spectral  
400 range is considered, and wavelengths longward of 2500 nm contribute to the clustering as  
401 well. As we will see in Section 4.1, this also has an impact on the spatial distribution of the  
402 clusters. The color scale is associated with increasing reflectance of the transmission  
403 window at 1700 nm (cyan, red, orange, blue and green from low to high, indicating  
404 increasing opacity and variable crystal sizes). The same color scheme is retained for the  
405 intensity of Fresnel peak at 3100 nm (Figure 8C), diagnostic of the ice crystallinity. Instead,  
406 spectra with intermediate reflectances at 1700 nm switch order within the 3700 nm ice  
407 reflectivity peak (red to blue to orange from low to high, Figure 8C) indicating the increased  
408 weight of thermal emission on the overall signal in this range. At  $\lambda > 4500$  nm (Figure 8D) the  
409 initial color scheme is totally disrupted, due to the mixing of information about cloud  
410 emissivity, cloud temperature (i.e. the altitude) and gaseous opacity. The combination of high  
411 NIR reflectances and low thermal emission (green cluster) suggests the presence of optically  
412 thick high-altitude clouds, as confirmed by the shallower water absorption bands longward of  
413 4900 nm. On the other hand, large thermal radiance and deep water bands associated with  
414 intermediate NIR reflectance (red cluster) indicate a population of moderate opacity clouds at  
415 quite low altitudes. The other clusters present intermediate properties in the thermal range,  
416 not strongly correlated with the NIR reflectance, calling for mixed-phase clouds of variable  
417 microphysical properties and vertical structure.

418



419 **A**  
 420 **B**  
 421 **C**  
 422 **D**

423 **Figure 8:** **A:** mean reflectance spectra from the K-means clustering algorithm for MAJIS  
 424 cube C16 ( $\lambda < 2500$  nm, wavelengths saturated due to the high reflectivity of clouds are  
 425 highlighted by the red shaded area). Colors are ordered with increasing reflectance of the  
 426 1700 nm transmission window (from cyan to green) **B:** same as in A but for PRISMA session  
 427 04 (full spectral range). The insets in **A** and **B** zoom between 1570 and 1780 nm to show the  
 428 average 1650 nm band normalized to the continuum. **C:** MAJIS radiances in the  $2800 < \lambda <$   
 429 4200 nm range, zooming on the Fresnel and 3700 nm ice reflectivity peaks. **D:** thermal part  
 430 of the spectrum longward of 4400 nm. In all panels, dashed arrows highlight diagnostic  
 431 spectral features of the ice.

432

### 433 3.3. Estimation of clouds' altitude

434

435 The most straightforward method for evaluating cloud altitudes involves the correlation of the  
 436 brightness temperature at a given wavelength (e.g. 4610 nm, less affected by gaseous  
 437 absorption in the MAJIS range) with a known vertical temperature profile. For ice clouds,  
 438 temperatures can be derived from the 3700 nm peak position (Section 3.3.3). Other methods  
 439 that we consider here are based on  $O_2$  absorption bands' variability and on the analysis of  
 440 clouds' shadows (Sections 3.3.1 and 3.3.2). In this study, we rely on a fixed average  
 441 temperature profile (Efremenko and Kokhanovsky, 2021), which may be not representative  
 442 of the actual thermodynamic conditions of the atmosphere during the observations. As a  
 443 consequence, all the methods that we adopt yield a range of results, each affected by their  
 444 own intrinsic limitations. Although they appear quite consistent with each other, more  
 quantitative investigations are postponed to future analyses.



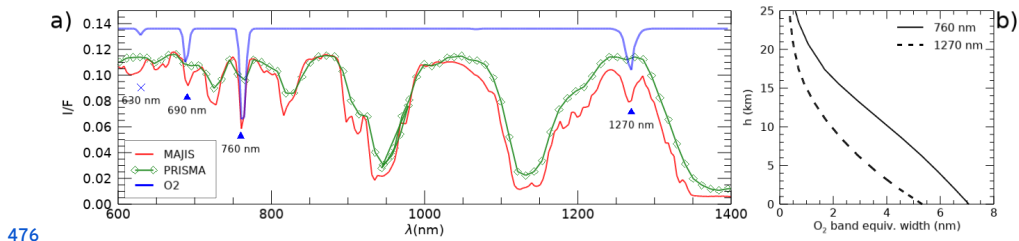
445                   **3.3.1. *O<sub>2</sub> band depth variability***

446

447 The O<sub>2</sub> spectral features covered by both MAJIS and PRISMA observations consist of the  
 448 absorption bands at 630 nm, 690 nm, 760 nm and 1270 nm (Newnham & Ballard, 1998;  
 449 Smith & Newnham, 1999). As we can see in Figure 9A, MAJIS can resolve all bands except  
 450 the 630 nm one, while PRISMA data can only partially resolve the 760 nm one. The  
 451 strongest 760 nm band is the most used from satellite measurements in the near-infrared  
 452 (e.g. GOSAT, Butz et al., 2011; SCIAMACHY, Bovensmann et al., 1999; TROPOMI, Veefkind  
 453 et al., 2012; OCO-2/3, Eldering et al., 2019) for inferring bulk atmospheric quantities like  
 454 temperature profile, airmass (Stevens et al., 2017), aerosol and clouds properties (Geddes &  
 455 Bösch, 2015). O<sub>2</sub> is a well-mixed component of the atmosphere, hence the curves of growth  
 456 of its absorption bands with altitude in the presence of optically thick clouds can be  
 457 translated into the altitude of the cloud top (e.g. Wei et al., 2024).

458 In our analysis we applied a simplified scheme for retrieving cloud top altitudes from the 760  
 459 nm band in the PRISMA case and from both 760 and 1270 nm O<sub>2</sub> bands for MAJIS data.  
 460 The different strength of the two bands implies a bit different curve of growth with altitude  
 461 (Figure 9B), with the 1270 nm one less sensitive to higher clouds but more suitable for  
 462 characterizing lower structures. The 630 and 690 nm bands, intrinsically weaker and more  
 463 sensitive toward the surface, are not used in this analysis.

464 The comparison of a measured O<sub>2</sub> band depth with its theoretical curve of growth, evaluated  
 465 for the actual airmass, allows us to directly retrieve the cloud top altitude (Section 4.2.1). It is  
 466 worth stressing that although altitude, pressure and temperature of the cloud top are  
 467 important atmospheric parameters (Nakajima et al., 2019), our simplified scheme neglects  
 468 details of vertical distributions and scattering properties, introducing possible biases in the  
 469 retrieved absolute values. Propagating the MAJIS uncertainties previously discussed  
 470 (Section 2.3.1) and assuming suitable model ones (~10% on the oxygen vertical profile  
 471 induced by local changes in gaseous temperature, density, humidity), errors on cloud top  
 472 altitude average to values of ~1 km, for both the 760 and 1270 nm bands. In addition, the  
 473 1270 nm band is known to contain a significant airglow emission feature that can alter the  
 474 band depth and introduce further biases in the oxygen absorption evaluation (Kuang et al.,  
 475 2002).



476

477 Figure 9: **A:** Typical appearance of O<sub>2</sub> features in the spectra of MAJIS (red) and PRISMA  
 478 (green). Modeled spectral transmittance (in blue) highlights location and shape of the O<sub>2</sub>  
 479 bands at 630, 690, 760, and 1270 nm. Only the last three can be appreciated in MAJIS  
 480 spectra (red curve), while only the strongest 760 nm band is identifiable in PRISMA spectra  
 481 (red curve). **B:** Curves of growth of the O<sub>2</sub> bands at 760 (solid curve) and 1270 nm (dashed  
 482 curve) in the standard atmospheric column adopted in this work.

483

484                   **3.3.2. *Cloud shadows analysis***



485

486 Significant lengths of projected shadows are more easily seen in the case of convective  
487 clouds in slant solar illumination. In the MAJIS case, clear shadows have been identified for  
488 strong convective events surrounded by widespread background clouds, hence their length  
489 can only give hints on relative altitudes (see Section 4.2.2). Uncertainties in this kind of  
490 measurements are mainly driven by errors in edge detection (for both cloud and shadow  
491 edges), limited by the spatial resolution. Errors on solar incidence angle may also play a role  
492 in very slant illumination, and the total relative uncertainties estimated in the conditions of  
493 MAJIS observations range between 6 and 10%.

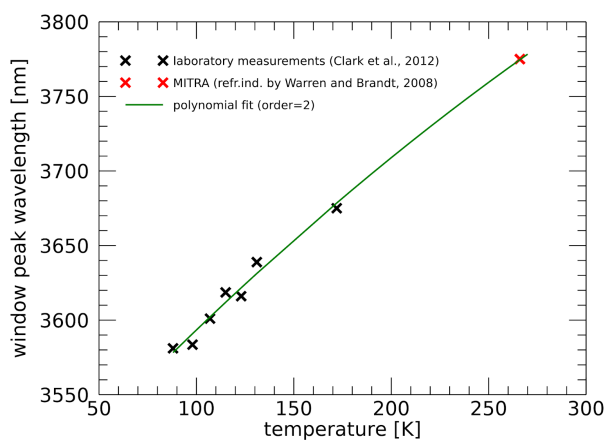
494

### 495 3.3.3. Derivation of clouds' altitude with the ice temperature

496

497 We apply to Earth's icy clouds the same method by Filacchione et al. (2016), who estimated  
498 the temperatures of Saturn's icy satellites surfaces from the displacement of the 3700 nm ice  
499 peak, deriving from a shift of the imaginary part of the ice refractive (Mastrapa et al., 2009).  
500 In that method, temperature-dependent peak reflectivities were derived from laboratory  
501 measurements by Clark et al. (2012), spanning between 88 and 172 K, a range too low to  
502 describe Earth troposphere where clouds are commonly observed. We extrapolate the  
503 peak-temperature dependence by also simulating the ice reflectivity at 266 K, i.e. the  
504 temperature of the optical constants by Warren and Brandt (2008). Since the ice grain size  
505 has little effect on the peak position (Filacchione et al., 2012) we assume an effective radius  
506 of 20  $\mu\text{m}$ , representative of cirrus clouds (LeMone, 1988). The resulting trend covering from  
507 88 to 266 K is shown in Figure 10 (black and red crosses). It is reliably fit with a  
508 second-degree polynomial (green line) and can be used for a qualitative estimation of the ice  
509 temperature in MAJIS observations (Section 4.2.3).

510



511

512 **Figure 10:** correlation between ice temperature and 3700 nm reflectivity peak position. Black  
513 crosses represent laboratory measurements by Clark et al. (2012), the red cross indicates an  
514 RT simulation performed with ice grain size of 20  $\mu\text{m}$  and optical constants by Warren and  
515 Brandt (2008), and the green line represents a second degree polynomial fit of all data (see  
516 Section 3.3.3).



517

### 518        **3.3.4. Forward RT modeling on liquid and ice H<sub>2</sub>O clouds;**

519

520 The most accurate method for determining clouds' vertical distribution is through full RT  
521 modeling. However, this would require a time-consuming retrieval of physical quantities that  
522 is beyond the scope of this paper. Instead of spectral inversion, we here perform a  
523 comparison of selected observations (those in Figure 3) with forward RT models obtained by  
524 manually tuning aerosols' physical parameters. The derived quantities are to be considered  
525 as orders of magnitude of the altitude and microphysical properties of Earth's clouds and  
526 aerosols. Forward models are produced with the MITRA RT tool (Oliva et al., 2016; 2018;  
527 Sindoni et al., 2017; D'Aversa et al., 2022), exploiting the optical constants from Hale and  
528 Querry (1973), Warren and Brandt (2008) and Kitamura et al. (2007) for computing the  
529 scattering properties of liquid water, water ice and silicate minerals (assumed as background  
530 aerosol), respectively. The spectral albedo of the ocean is taken from the ASTER spectral  
531 library (Baldridge et al., 2009). In this simplified scheme, we neglect thermal emission,  
532 discarding measurements longwards 3000 nm.

533 It is interesting to note that, even if beyond the scope of this paper, more accurate RT  
534 modeling could also be exploited for the evaluation of straylight contamination (studied for  
535 MAJIS in Langevin et al., this issue), as it offers the possibility to extrapolate information  
536 from the NIR part of the spectrum to visible wavelengths.

537

### 538        **3.4. High altitude emissions and atmospheric waves identification**

539

540 Among the many gaseous features observable in the 4000-5500 nm MAJIS range, two are  
541 particularly interesting, being observed as emission bands: the CO<sub>2</sub> double-peak at the  
542 bottom of the main 4300 nm band and an O<sub>3</sub> signature around 4700 nm. Both are evident  
543 above optically thick clouds at high altitudes, blocking the thermal contribution from the  
544 surface and lower (hotter) atmospheric layers. The CO<sub>2</sub> peak is radiometrically much more  
545 stable than other spectral features against variation of atmospheric structures (see Poulet et  
546 al., this issue). It is known to result from the combination of a LTE component induced by  
547 temperature increase in the stratosphere, and a non-LTE one due to the CO<sub>2</sub> excitation  
548 primarily induced by direct solar pumping occurring at even higher altitudes (where  
549 collisional quenching is no longer efficient, e.g. Cassini et al., 2025). The detailed analysis of  
550 this emission feature in MAJIS data, implying the evaluation of CO<sub>2</sub> vibrational temperature  
551 vertical profiles, is far beyond the purpose of this work. In any case, the spatial distribution of  
552 the CO<sub>2</sub> emission intensity can provide interesting insights about the probed layers, and we  
553 can indeed use it for detecting atmospheric waves and provide hints about their altitude and  
554 propagation (see Section 4.3.1). CO<sub>2</sub> emission can be identified already in MAJIS  
555 monochromatic frames at 4270 nm (i.e. the position of the main peak of the emission) but  
556 the integration of the band in a narrow spectral range is useful for reducing noise and  
557 enhancing the contrast in waves' investigation (Section 4.3). For the integration we consider  
558 wavelengths between 4254 and 4333 nm, which probe high altitudes in the atmosphere and  
559 are not affected by the thermal contribution from lower ones. Considering the SNR estimated  
560 at these wavelengths (Figure 3C), we are able to detect waves whose relative intensity  
561 between crests and troughs is about 1%, assuming a 3-sigma uncertainty for the radiance at  
562 4270 nm.

563 On Earth ozone has a maximum density in the lower stratosphere but its vertical distribution  
564 strongly depends on latitude (see for example Bekki and Lefevre, 2009). It is produced



565 through a very fast and exothermic 3-body recombination reaction that includes O and O<sub>2</sub> in  
566 the presence of a catalytic species (either N<sub>2</sub> or O<sub>2</sub>). Aside from diagnostic bands at UV  
567 (outside MAJIS domain) and VIS wavelengths (the Chappuis band discussed in Section  
568 2.3.2), the 4700 nm one is the strongest feature clearly detectable within the MAJIS range.  
569 This O<sub>3</sub> band is seen as either an absorption or emission feature in MAJIS nadir-looking  
570 observations, depending on the overall thermal emission of the atmospheric column. In clear  
571 sky conditions, when the emission from lower warmer layers is dominant, the O<sub>3</sub> 4700 nm  
572 band is hardly detectable, being overcome by water absorption as shown in Poulet et al. (this  
573 issue). In the presence of mid-altitude clouds, a shallow O<sub>3</sub> band appears in absorption,  
574 while the obstruction of the densest part of the atmospheric column due to high-altitude  
575 clouds makes the O<sub>3</sub> band appear in emission. Given this phenomenology, in this preliminary  
576 study we investigate the O<sub>3</sub> emission amplitude through the difference between brightness  
577 temperatures estimated at 4717 nm (strongest O<sub>3</sub> line) and 4660 nm (outside O<sub>3</sub> band). Such  
578 a difference is positive when the O<sub>3</sub> is spectrally observed in emission, negative otherwise.

579

580

### 581           **3.4.1. Atmospheric waves characterization**

582

583 Atmospheric gravity waves are observed in almost all the MAJIS acquisitions (see examples  
584 in Section 4.3.1) at the wavelengths of the central peak of the 4300 nm CO<sub>2</sub> band. Due to the  
585 limited field of view, wave packets are usually not visible in their entirety and it is not possible  
586 to identify the same wavy structures from one image to the other due to the large coverage  
587 gaps, preventing the study of the wave speed propagation. Nevertheless, we attempt to  
588 quantify wave properties and provide some hints on their altitude. We investigated the  
589 wavelength, the total length of the packet, the azimuth angle of the direction of propagation  
590 (anticlockwise), and the extension of the observed wavefront (packet width). Taking into  
591 account spatial resolution and signal contrast, uncertainties in size estimation are of about 7  
592 km, while those on wavelengths are less than about 11 km.

593 Circular-wave patterns have been observed in some MAJIS images, likely resulting from the  
594 breaking of upward-propagating waves originating in sufficiently strong convective  
595 thunderstorms. Under this assumption, we attempt to infer the time delay between the  
596 wave-triggering event and its observation (Taylor and Hapgood, 1988; Dewan et al., 1998;  
597 see Section 4.3.1). This is done neglecting wind transport and assuming a simplified  
598 isothermal dispersion relation (Hines, 1960) in which the wave speed is negligible with  
599 respect to the speed of sound. For circular waves we also measured maximum radius and  
600 expansion speed. The latter depends on the measured length and period, as well as on the  
601 buoyancy period  $\tau_B$ , for which a value of 5 min can be assumed as a good approximation at  
602 stratospheric altitudes (Dewan and Good, 1986).

603

## 604           **4. Results and discussion**

605

606 We now present the results we obtain through the application of the methods discussed in  
607 Section 3. Section 4.1 provides a discussion on ice properties, Section 4.2 focuses on the  
608 clouds' altitudes, Section 4.3 is devoted to high altitude features and Section 4.4 presents  
609 results on land features identification.

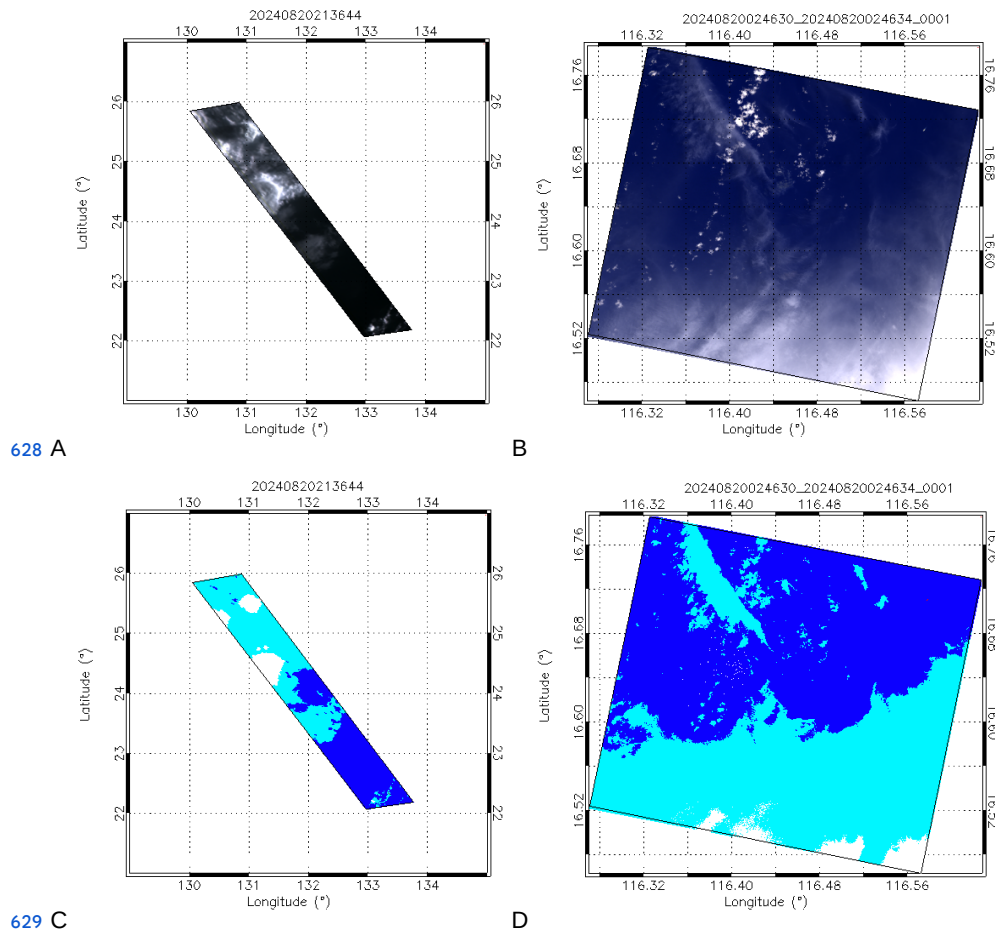
610

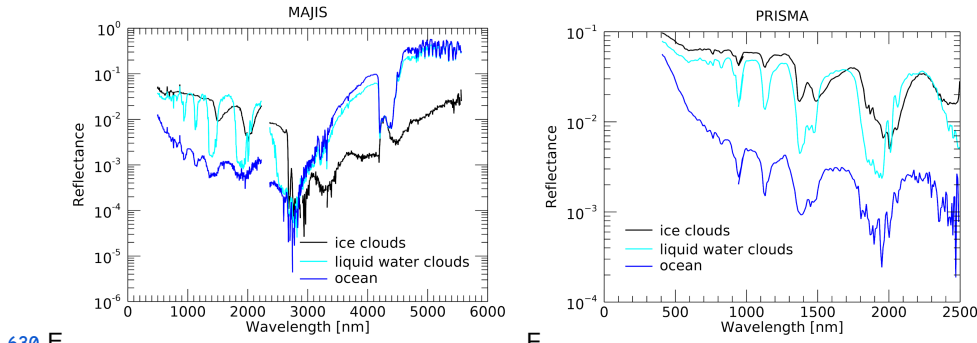
### 611           **4.1. Icy clouds properties**

612



613 Examples of two MAJIS and PRISMA cubes containing ice clouds, identified through the ice  
614 spectral index in Table 3 (threshold < 1), are given in Figure 11. In the MAJIS case, ice is  
615 found in localized convective clouds (Figure 11B and C), so high with respect to the  
616 background structures that they even cast well detectable shadows (see Section 4.2.2).  
617 Instead, in the PRISMA observation ice is detected both in diffuse bright clouds (e.g. at the  
618 southern east corner of Figure 11B and D) and in thinner and less contrasted structures  
619 (probably identifiable as high altitude cirrus clouds, e.g. the white regions around longitude  
620 116.4° - latitude 16.5°, Figure 11B and D) hence proving the effectiveness of the index with  
621 different regimes of ice optical depth. Sample spectra from the identified classes are shown  
622 in Figure 11E and F for MAJIS and PRISMA respectively. It must be noted that the very low  
623 albedo of the ocean in MAJIS spectrum at visual wavelengths (<1%) is due to the very slant  
624 illumination conditions for the selected observation (incidence angle of about 80° for cube  
625 C7, see Table 1). On the other hand, the spectra in the thermal range show consistency with  
626 the expected temperature regimes, with very cold ice clouds and the ocean hotter than liquid  
627 water clouds.





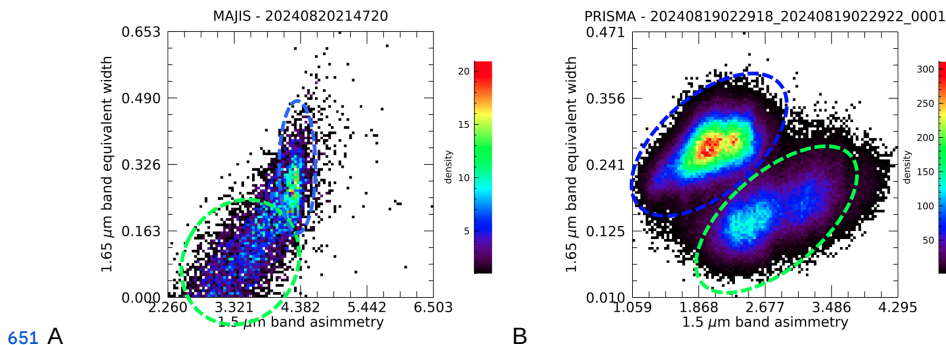
630 E

F

631 **Figure 11:** Panels **A** and **B** refer to MAJIS cube C7 and one of the PRISMA cubes from  
 632 session 07 respectively, displayed in RGB. Panels **C** and **D** show the masks for the detection  
 633 of ocean (blue), liquid water clouds (cyan, from the “cloudy” condition in Table 3) and ice  
 634 clouds (white) pixels related to the two cubes. Panels **E** and **F** display sample spectra related  
 635 to the different classes identified in MAJIS and PRISMA observations.

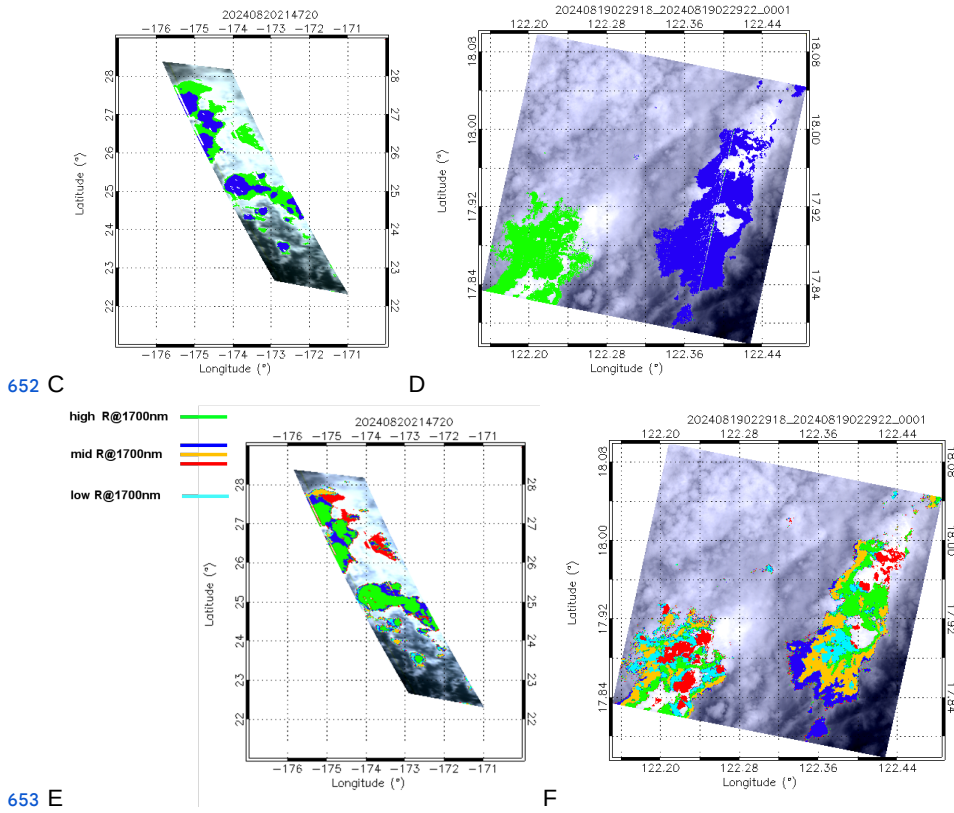
636

637 Ice is similarly widespread in other MAJIS and PRISMA data, so that some considerations  
 638 on its distribution and correlations of its parameters can be made (Figure 12). We compute  
 639 the 1500 nm band asymmetry as a ratio of slopes, the first considered between 1415 and  
 640 1500 nm (left wing) and the second between 1500 and 1790 nm (right wing). The asymmetry  
 641 correlates with the strength of the 1650nm band (quantified as equivalent width, Figure 12A  
 642 and B), with higher values indicating increasingly crystalline ice (Mastrapa, 2008; Stephan et  
 643 al. 2021; Grundy & Schmitt 1998). Different regimes of these two parameters map localized  
 644 structures in MAJIS and PRISMA observations, as shown in Figure 12C and D respectively  
 645 where green and blue pixels refer to clusters contained within dashed ellipses sharing the  
 646 same color in Figure 12A and B. In MAJIS case, the blue cluster is characterized by an  
 647 increasing 1650 nm equivalent width at constant 1500 nm band asymmetry. The green  
 648 cluster, instead, shows a common trend of growth for the two parameters. On the other  
 649 hand, the PRISMA ellipses identify well separated clusters of points within the two  
 650 parameters’ space.



651 A

B



652 C

D

653 E

F

654

655 Figure 12: **A-B:** scatterplots of the 1500 nm band asymmetry and the 1650 nm band  
656 equivalent width for MAJIS reflectance cube C16 and one of the PRISMA reflectance cubes  
657 from session 04. The colored-dashed ellipses separate different regimes of the two  
658 parameters (see Section 3.5). **C-D:** green and blue pixels map the clusters contained within  
659 the respective ellipses in panels A and B. **E-F:** clustering of ice observations obtained  
660 through the K-means classification algorithm (see Section 3.2).

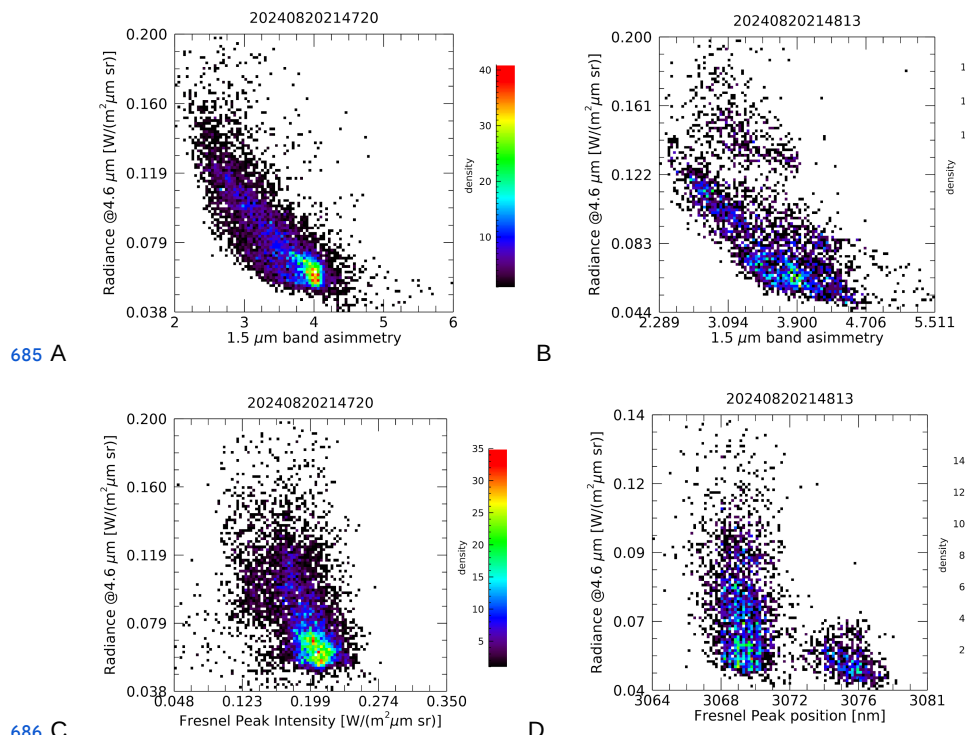
661

662 It is interesting to note that the correlation between these clusters and those obtained from  
663 the K-means classification discussed in Section 3.2 (Figure 12E-F) is not straightforward. For  
664 MAJIS, ice spectra with high reflectivity in the solar part of the spectrum (green in Figure  
665 12E) are mostly correlated with the blue cluster in Figure 12C. This trend is not observed in  
666 PRISMA, where all K-means clusters are equally distributed over both the blue and green  
667 clusters shown in Figure 12D, suggesting variable ice densities and grain sizes within the  
668 same regimes of crystallinity. This difference derives from the fact that, as explained in  
669 Section 3.2, for MAJIS the thermal wavelengths contribute to the K-means classification of  
670 the spectra, hence providing information also on the temperature of the ice (see also Section  
671 4.2.3). This is verified by the trend of the 1500 nm band asymmetry with the radiance in the  
672 thermal part of the spectrum, shown for MAJIS cubes C16 and C17 in Figure 13A-B: more  
673 crystalline ice (larger asymmetry) is correlated with lower radiances (i.e. temperatures) at  
674 thermal wavelengths. In particular, orbit C17 also shows a detached cluster in the distribution



675 of the thermal radiance suggesting different regimes of temperature (hence different clouds'  
 676 altitude). Finally, we show the correlation between the ice crystallinity and its temperature in  
 677 Figure 13C-D, where the intensity and wavelength of the Fresnel peak are compared to  
 678 MAJIS thermal radiances. Consistently with previous studies (e.g. Stephan et al., 2021), the  
 679 intensity of Fresnel peak is higher when the temperature is low (Figure 13C), indicating  
 680 enhanced crystallinity (see also Poulet et al., this issue). The comparison in Figure 13D  
 681 shows two distinct regimes of the peak position, with the short wavelength cluster  
 682 characterized by a larger spread of the thermal radiance (suggesting an enhanced  
 683 temperature variability for a less crystalline ice, e.g. Stephan et al., 2021).

684



685 A  
 686 B  
 687 C  
 688 D  
 689 Figure 13: **A-B:** scatterplots of the 1500 nm band asymmetry and thermal radiances at 4600  
 690 nm for MAJIS orbit C16 and C17 respectively. **C:** scatterplot of the Fresnel peak intensity  
 691 with the thermal radiance at 4600 nm for MAJIS orbit C16. **D:** scatterplot of the Fresnel peak  
 692 wavelength with the thermal radiance at 4600 nm for MAJIS orbit C17.

693

## 694 4.2. Clouds' altitude

695

696 We now discuss the altitudes of clouds derived with the different methods presented in  
 697 Section 3.3.

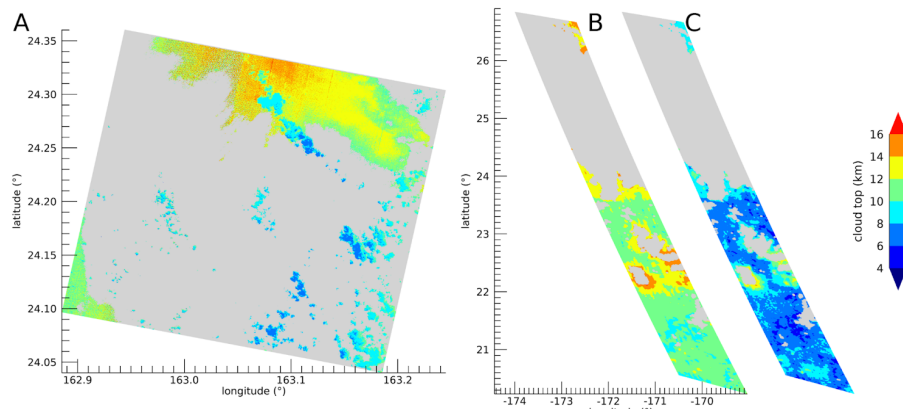
698

### 699 4.2.1. Altitudes from O<sub>2</sub> band depths



699 Figure 14 shows maps of cloud top altitude obtained applying the  $O_2$  bands' investigation  
700 method (Section 3.3.1) to sample PRISMA and MAJIS cubes. Taking into account the  
701 uncertainties of both datasets, the majority of altitudes derived from the 760 nm band are in  
702 remarkable agreement between MAJIS (modal value of  $11 \pm 1$  km, Figure 14A) and PRISMA  
703 (modal value of  $12.5 \pm 1.0$  km, Figure 14B), even if the observing angles were very different in  
704 the two cases ( $>60^\circ$  for MAJIS,  $\sim 12^\circ$  for PRISMA). A second lower-altitude population  
705 peaking at  $\sim 9$  km is only observed in PRISMA data, appearing as localized small structures  
706 that could remain unresolved if also present in the MAJIS scene (see Section 2.3.1). A more  
707 systematic discrepancy is obtained from cloud top altitudes through the 1270 nm band,  
708 whose modal value in MAJIS cube peaks as low as  $7.2 \pm 1.0$  km. This is expected, as this  
709 band is more sensitive to lower altitudes (Section 3.3.1) and we are neglecting cloud top  
710 scattering properties in evaluating the reflectance in the bottom of the bands. Such an issue  
711 can be resolved with proper radiative transfer modeling as suggested by the benchmark  
712 presented in Section 4.2.4.

713



714

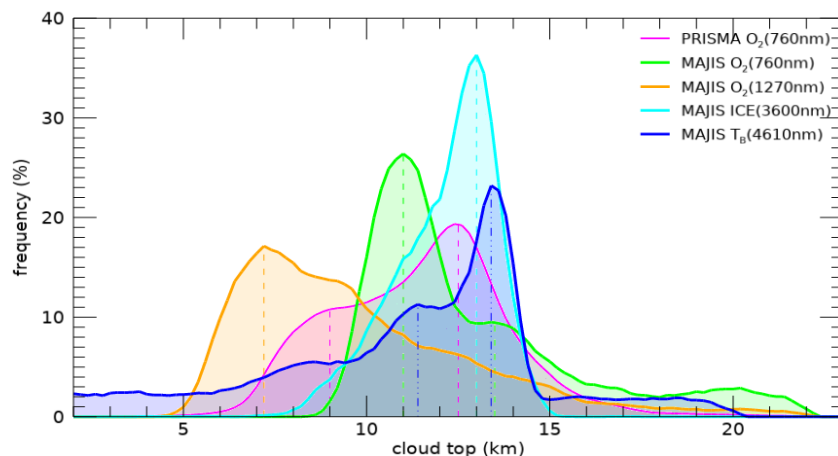
715 Figure 14: **A)**: Map of cloud top altitude retrieved through the  $O_2$  760 nm band in a PRISMA  
716 sequence 09 cube (20240820234657). Non-cloudy pixels or saturated ones are shown in  
717 grey. **B)**: the same as panel A but from a MAJIS data cube C17. **C)**: cloud top map for the  
718 same data in panel B (offset for clarity) but retrieved from the 1270 nm  $O_2$  band.  
719 Uncertainties are of the order of 1 km (Section 3.3.1).

720

721 The frequency distribution of top cloud altitudes derived from the same maps in Figure 14 is  
722 shown in Figure 15. The  $O_2$  760 nm band provides altitudes in good overall agreement  
723 between MAJIS and PRISMA (green and magenta curves), characterized by two main peaks  
724 around 11 km and 13 km. These are also the most frequent altitude values suggested by the  
725 thermal emission at 4610 nm (blue curve in Figure 15). The appearance of secondary peaks  
726 reflects intrinsic differences in the distribution of clouds in the observed scenes. The  
727 displacement between the peaks of the green and blue curves is expected due to  
728 assumptions in the clouds' albedo and emissivity in our qualitative estimate. Indeed, the  
729 adopted values of 1 for both quantities imply underestimation of clouds' altitudes from the  
730 760 nm  $O_2$  band depth, and overestimation from thermal brightness. This suggests that, if



731 proper radiative transfer modeling is considered, convergence of the peaks towards a  
732 common regime is possibly achieved. A similar effect is observed in the distribution of  
733 altitudes derived from the 1270 nm band depths, which are biased towards low values. The  
734 underestimation arising from the neglecting of scattering effects is magnified here, being the  
735 band even weaker than the 760 nm one. Moreover, non-LTE emission also plays a  
736 non-negligible effect in this band, further biasing the derived altitudes (see Section 3.3.1).  
737 Finally, we compare these distributions with that deriving from the ice temperature estimation  
738 method (Figure 15 cyan curve, see Section 3.3.3). This provides results (discussed in detail  
739 in Section 4.2.3) which are consistent with the other curves and indicates that the altitudes  
740 identified in the peaks of all distributions are likely related to observations containing ice.



741  
742 Figure 15: Comparison of cloud top altitudes retrieved from PRISMA and MAJIS session 09  
743 and C17 cubes respectively, through different methods. Distributions related to the maps in  
744 Figure 14A, B, C, derived from  $O_2$  band depths, are shown in magenta, green, and orange  
745 colors respectively. Cyan curve refers to ice clouds only (method described in Section 3.3.3  
746 and discussed in Section 4.2.3), while the distribution obtained from thermal emission at  
747 4610 nm (for cloudy pixels only) is given by the blue curve.

748

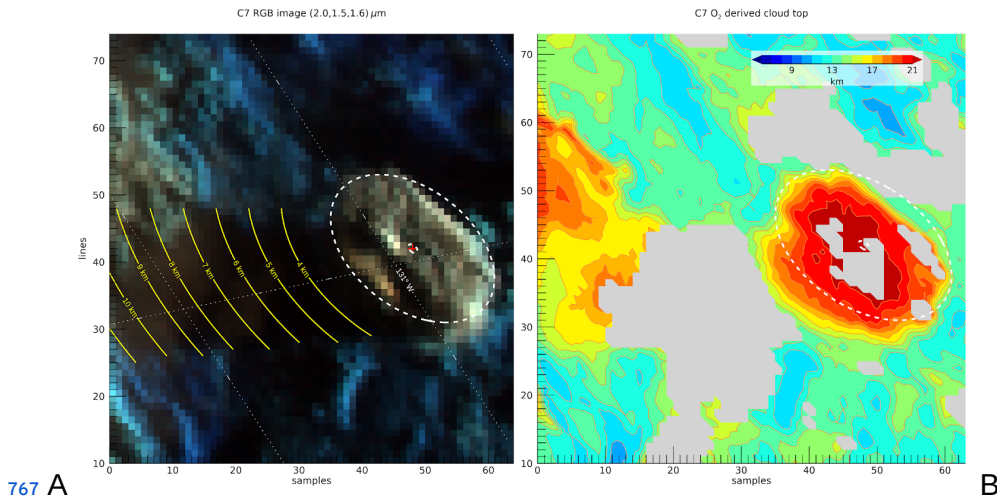
#### 749 4.2.2. Altitudes from clouds' shadows

750

751 An example of the results obtained from the method described in Section 3.3.2 is given in  
752 Figure 16, where the shadows projected by high convective anvil clouds are clearly visible in  
753 MAJIS data cube C7. The grazing illumination of the scene (incidence angle  $\sim 80^\circ$ ) enables a  
754 vertical resolution of  $\sim 0.7$  km, inferred from uncertainties of  $\sim 0.5^\circ$  on incidence angles and  
755 2.7 km on shadow length (about twice the horizontal spatial resolution). Within this  
756 framework, the horizontal length of the shadow translates to a top altitude of about 10 km  
757 (see yellow lines). Of course this value is not absolute but only an estimate relative to the  
758 surrounding decks, whose altitudes can be qualitatively inferred through the estimation of the  
759  $O_2$  760 nm band depth (see previous section). The  $O_2$ -derived elevations are shown in the  
760 map of Figure 16B, where the background structures appear to be located around 11 - 12



761 km, while the anvil cloud top peaks at  $\sim$  21 km. This implies a differential height of  $\sim$  10 km  
762 between the anvil and the surrounding clouds, in very good agreement with the estimated  
763 shadow length. Of course, the absolute height of the cloud top can only be derived if multiple  
764 scattering effects are accounted for in the reproduction of the 760 nm  $O_2$  band.  
765 Nevertheless, the shadow analysis provides a quick and robust way for estimating the  
766 relative height of isolated structures with respect to their background.



767 **Figure 16:** A): Example of cloud top altitude estimation based on projected shadow length in  
768 the MAJIS data cube C7. The yellow isolines refer to cloud altitudes, while the white dashed  
769 line approximately indicates the cloud boundaries (center indicated by the red dot). B):  
770 Comparison with the cloud top altitudes retrieved from  $O_2$  760 nm band (see Section 4.2.2).  
771 In both panels 'samples' indicate the spatial pixels in the slit, while 'lines' refer to adjacent  
772 acquisitions of the slit in the cube.

773

#### 774 4.2.3. Altitudes from ice temperature

775

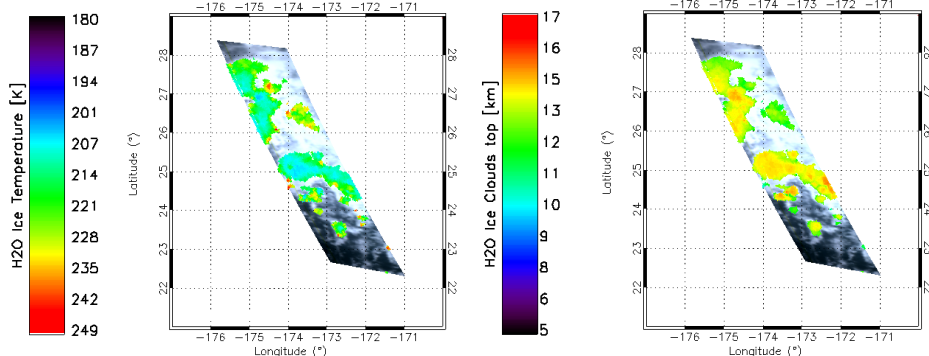
776 In Figure 17 we show two examples of the temperature and altitude maps derived with the  
777 method described in Section 3.3.3, for MAJIS cubes C16 (panel A) and C17 (panel B).  
778 Altitudes are derived by assuming that the clouds are in thermal equilibrium with the  
779 surrounding air and reside within the troposphere, where the temperature vertical lapse rate  
780 is positive. Altitudes' errors are of about 1 km (Section 3.3.1) while those related to  
781 temperatures are propagated from the 3700 nm peak uncertainties (Table 4) and result of  
782 about 1 K. Orbit C16 (Figure 17A) shows two main decks, placed respectively at  $z \sim 15$  km  
783 and  $z \sim 12$  km which can be compared with the maps in Figure 12C and E, where the 1650  
784 nm band depth and K-means clusters are shown. The higher deck at  $z \sim 15$  km correlates  
785 with the blue cluster in Figure 12C and the green one in Figure 12E, suggesting increased  
786 opacity and crystallinity at lower temperatures.

787 Similarly, two regimes of temperatures and altitudes are found in orbit C17, with higher  
788 clouds at  $z \sim 15$  km ( $T \sim 205$  K) and lower ones at  $10 < z < 12$  km ( $215 < T < 250$  K). As  
789 suggested by the scatterplot in Figure 13D, these two decks are characterized by different  
790 ice properties. Indeed, the short wavelength Fresnel peak cluster (i.e. reduced crystallinity,  
791 Cartwright et al., 2025) shows a larger spread of temperatures, consistent with the lower

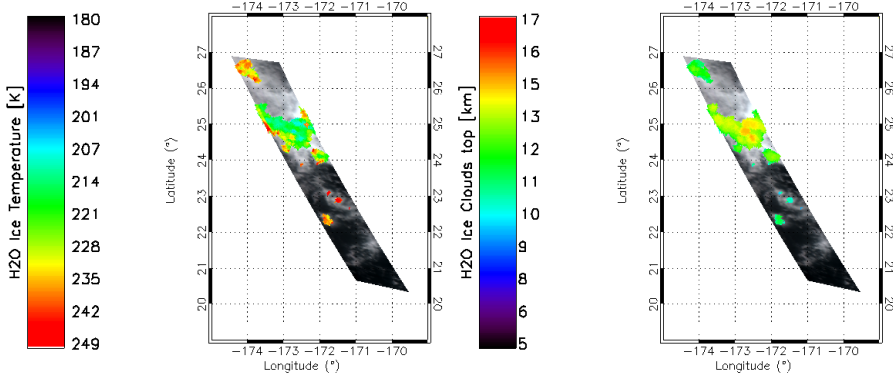


793 clouds discussed here. Instead, the long wavelength Fresnel peak cluster shows overall  
 794 lower thermal radiances, and hence temperatures, in agreement with the higher clouds  
 795 identified at  $\sim 15$  km (see also Poulet et al., this issue).

796



797 A



798 B

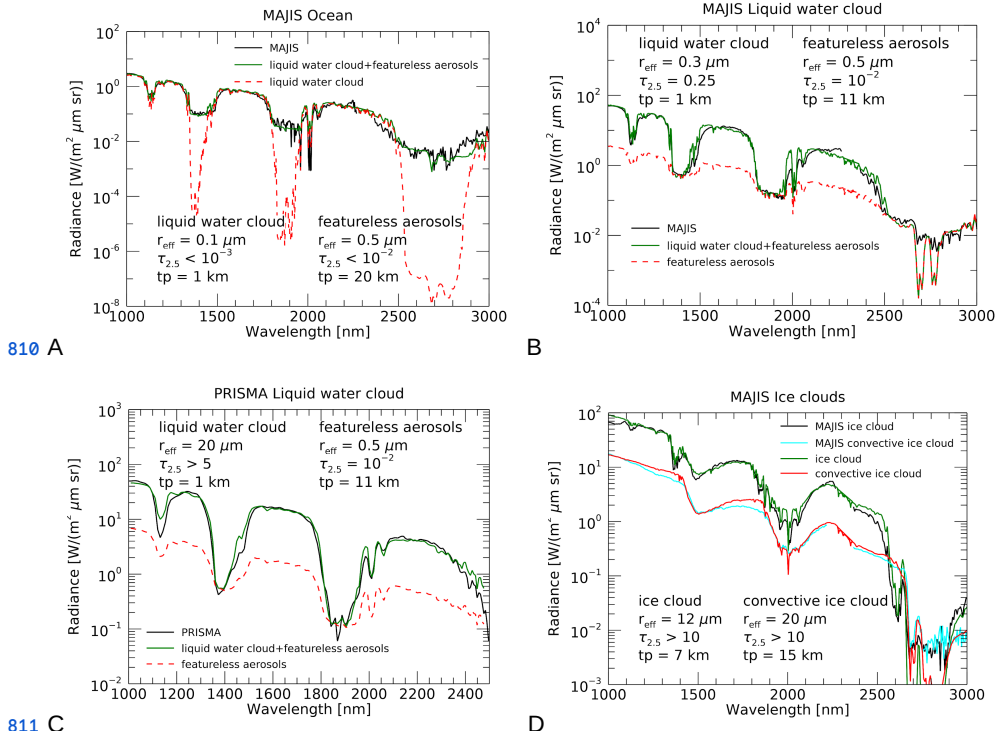
799 **Figure 17:** ice temperature (left) and inferred cloud altitude (right) mapped on MAJIS cube  
 800 C16 (**A**) and C17 (**B**). Ice is identified with a threshold  $< 1$  on the ice clouds condition in  
 801 Table 3.

802

#### 803 4.2.4. Results from RT modeling

804

805 For our forward RT modeling (Section 3.3.4) we consider all MAJIS spectra and the PRISMA  
 806 liquid water cloud one from Figure 3, as it is the one showing the most evident differences  
 807 with respect to its MAJIS counterpart. We also take into account a MAJIS ice cloud spectrum  
 808 related to one of the convective structures identified in Figure 11A-C and studied in Section  
 809 4.2.2.



812 **Figure 18:** Panel A: MAJIS ocean spectrum from Figure 3 is shown in black, its forward RT  
 813 fit is shown in green, while the contribution from the liquid water cloud in the simulation is  
 814 given in dashed red. Geometrical and microphysical parameters ( $r_{\text{eff}}$  is the effective radius in  
 815  $\mu\text{m}$ ,  $\tau_{2.5}$  is the optical depth at  $2.5 \mu\text{m}$  and  $tp$  is the cloud top in km) of aerosols involved in  
 816 the fit are given in the figure. Panels B-C: same as in panel A, but liquid water clouds  
 817 observations by MAJIS and PRISMA from Figure 3 are respectively fit. The dashed red lines  
 818 here refer to the contribution from the featureless aerosols in the model (i.e. when no liquid  
 819 water cloud is considered). D: MAJIS ice clouds forward RT fits (green and red lines) related  
 820 to MAJIS ice cloud spectrum from Figure 3 (black) and to a spectrum from the convective  
 821 cloud identified in Figure 11C (cyan line).

822

823 The best fits obtained with this approach are shown in Figure 18. In general, grain sizes and  
 824 clouds' altitudes determine the shape and the signal of water absorption bands, while the  
 825 number density can be tweaked to match the intensity of the continuum. We assume that the  
 826 clouds are compact in vertical extent and only occupy a single layer of the atmospheric  
 827 profile. The ocean and liquid water clouds observations require two separate layers placed  
 828 at different altitudes in the atmosphere (Figure 18A, B and C) suggesting that, as explained  
 829 in Sections 2.3.1 and 3.1, also the ocean spectra we are investigating are partially  
 830 obstructed by non-resolved cloudy structures. The lower layer shapes the shoulders of water  
 831 bands', in which the atmospheric transmission is enough to probe down to the surface, while  
 832 the upper one is needed to correctly model the intensity of the bands' bottom. Indeed, if  
 833 optically thick enough, high clouds prevent solar photons from reaching the underneath  
 834 atmospheric layers, hence reducing the gaseous absorption. Such a differential effect in the



835 models is shown as dashed red lines in Figure 18A, B, C. In the ocean spectrum (Figure  
836 18A) the optically thin bottom layer ( $z = 1 \text{ km}$ ,  $\tau < 10^{-3}$ ) with small grain sizes ( $r_{\text{eff}} = 0.1 \mu\text{m}$ ) is  
837 consistent with the average properties of maritime droplets ( $0 < z < 2 \text{ km}$ ,  $5 \times 10^{-4} < \tau < 10^{-3}$ ,  
838  $0.05 < r_{\text{eff}} < 1.5 \mu\text{m}$ ) commonly observed above the surface of the ocean (Croft et al., 2021;  
839 Smirnov et al., 2002; Heintzenberg et al., 2000). On the other hand, the upper thin layer ( $\tau <$   
840  $10^{-2}$ ) has slightly larger particles ( $r_{\text{eff}} = 0.5 \mu\text{m}$ ) and is placed at 20 km, in agreement with the  
841 presence of stratospheric background aerosols ( $15 < z < 25 \text{ km}$ ,  $10^{-4} < \tau < 10^{-3}$ ,  $0.1 < r_{\text{eff}} < 1$   
842  $\mu\text{m}$ , Voudouri et al., 2023; Thomason et al., 2008). Such a configuration confirms the  
843 observation as a partially obstructed scenario.

844 The selected MAJIS and PRISMA liquid water clouds observations (Figure 3 and Figure  
845 18B-C) show a good radiometric agreement but differences in water bands' shape that can  
846 be explained by changes in the aerosols' microphysical properties. Both observations are  
847 characterized by a high altitude, spectrally featureless, thin aerosol layer ( $tp = 11 \text{ km}$ ,  $\tau \sim 10^{-2}$ )  
848 that is required to reproduce the bottom of water bands. This indicates the presence of faint  
849 background stratospheric aerosols residing at the tropopause. Instead, the lower liquid water  
850 layer ( $z = 1 \text{ km}$ ) is thin with small grains in the MAJIS case ( $\tau = 0.25$ ,  $r_{\text{eff}} = 0.3 \mu\text{m}$ )  
851 suggesting spray marine boundary layer aerosols (Sun et al., 2023; Zheng et al., 2018; Luo  
852 et al., 2014), and thicker with large grains in the PRISMA case ( $\tau > 5$ ,  $r_{\text{eff}} = 20 \mu\text{m}$ ),  
853 consistent with the presence of stratus clouds (Fu et al., 2022; Rossow and Shiffer, 1999;  
854 LeMone, 1988). Hence, different properties ensure the modeling of flatter (MAJIS) and  
855 sharper (PRISMA) bands in the two observations.

856 The two ice observations (Figure 18D) are reproduced with a single cloud layer and do not  
857 require the lower one. This is because the ice clouds in the models have opacities so high ( $\tau$   
858  $> 10$ ) that they prevent observing the ocean and the atmospheric layers in between. In such  
859 conditions, the ice cloud in practice acts as a surface with high albedo, accounting for most  
860 of the spectral features in the observations. However, two different clouds' observations are  
861 considered here. The first one (black line in Figure 18D) is related to a small structure  
862 identified around longitude  $133^\circ$  and latitude  $22^\circ$  in Figure 11C. This cloud can be modelled  
863 with ice crystals of the order of  $10 \mu\text{m}$  in radius (green line). The altitude can be reliably  
864 tweaked by studying the depth of gaseous water absorption bands at  $1380 \text{ nm}$  and  $2600 \text{ nm}$ ,  
865 both identifiable in the observation. This means that the ice cloud is low enough to ensure  
866 some water absorption, before completely shielding the underneath atmosphere. As a result,  
867 our estimate is that it has its top at 7 km. These parameters suggest compatibility with the  
868 presence of a thick cirrus cloud ( $6 < z < 13 \text{ km}$ ,  $\tau > 3$ ,  $10 < r_{\text{eff}} < 60 \mu\text{m}$ , Baran, 2009; Zhou et  
869 al., 2017; LeMone, 1988).

870 The other ice cloud (cyan line in Figure 18D) is selected on the larger convective structure  
871 identified in Figure 11C. We already expect this to be higher in the atmosphere with respect  
872 to the other one (Section 4.2.2). Our model (red line) suggests that it is characterized by  
873 larger crystals ( $20 \mu\text{m}$ ) and reaches an altitude of at least 15 km, enough to prevent water  
874 absorption in the  $1380$  and  $2600 \text{ nm}$  bands (the model sensitivity to higher altitudes is  
875 reduced making this estimate a lower limit). These values indicate that in this observation  
876 MAJIS is probing the upper frozen top of a large convective cloud ( $8 < z < 16 \text{ km}$ ,  $\tau > 10$ ,  $10$   
877  $< r_{\text{eff}} < 60 \mu\text{m}$ , Dolan et al., 2023; Krisna et al., 2018; van Diedenhoven et al., 2018).

878

879

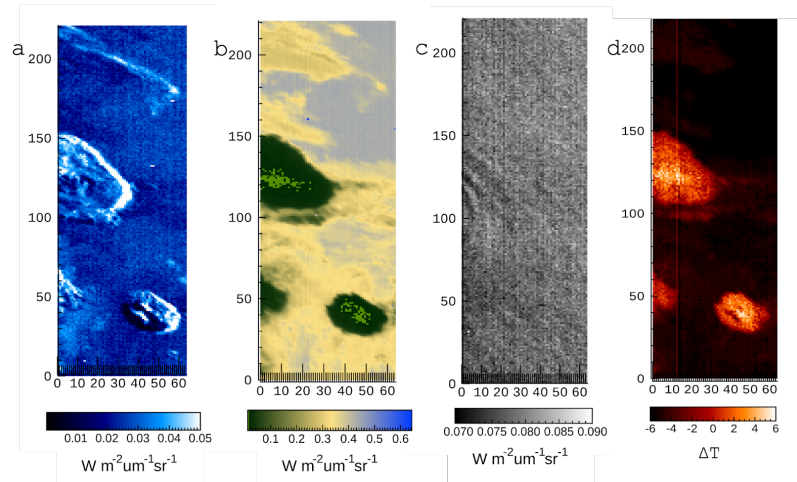
880       **4.3. Upper atmosphere features**

881



882 The CO<sub>2</sub> and O<sub>3</sub> emissions introduced in Section 3.4 have been studied in all MAJIS cubes,  
883 deriving maps like those shown in the examples of Figure 19 and Figure 20. In Figure 19,  
884 panels A and B show MAJIS cube C7 displayed at 3100 and 4512 nm, whose  
885 anti-correlation highlights the presence of the convective clouds discussed in Sections 4.1,  
886 4.2.2 and 4.2.4. Panels C and D, instead, show the radiance of the peak of CO<sub>2</sub> emission at  
887 4270 nm and the brightness temperature difference between the O<sub>3</sub> emission peak and its  
888 continuum (Section 3.4). It is evident how wavy patterns can be seen in the CO<sub>2</sub> map and  
889 are uncorrelated with the clouds beneath. No wave patterns are spotted from the O<sub>3</sub>  
890 emission, whose positive values (and hence the emission) are only detectable above the  
891 convective structures. This suggests that, while both phenomena are likely happening above  
892 the clouds' top, waves are generated at different altitudes with respect to those pertaining to  
893 the O<sub>3</sub> emission. However, the actual heights are not investigated here, since a rigorous  
894 retrieval accounting for non-LTE effects (required for the assessment of these high-altitude  
895 emissions) is beyond the scope of the paper.

896



897

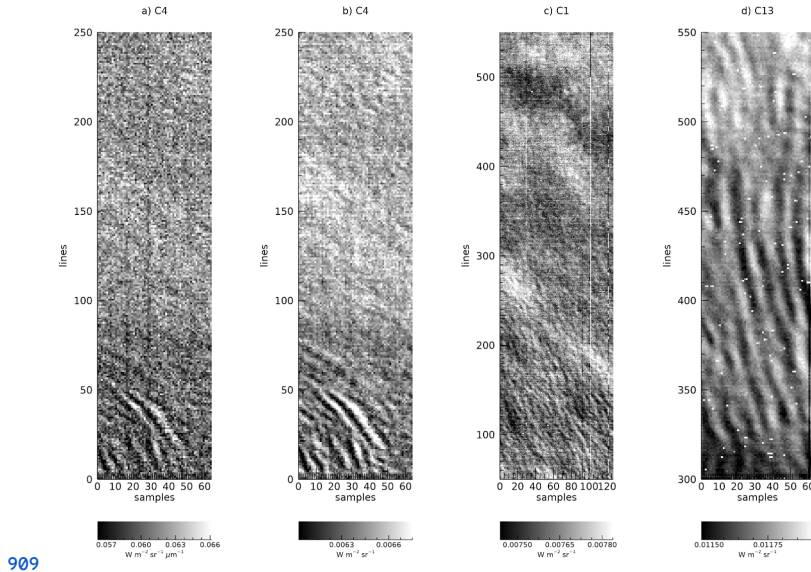
898

899 **Figure 19.** A-B: MAJIS cube C7 radiances at 3100 nm and 4512 nm respectively,  
900 highlighting the anti-correlation between enhanced ice content (A, i.e. larger reflectances of  
901 the Fresnel peak) and low thermal contribution (B). C: radiance of the CO<sub>2</sub> emission peak at  
902 4270 nm, in which the gravity wave pattern is identified. D: brightness temperature difference  
903 (in K) between the O<sub>3</sub> emission peak (4717 nm) and its continuum (4660 nm), showing  
904 positive values above the clouds. In all maps, the vertical axis indicates the number of lines  
905 while the horizontal axis indicates the number of samples.

906

907

908



909

910 **Figure 20.** A circular wave pattern is clearly observed in MAJIS C4 cube at 4270 nm (panel  
 911 a). Panel b shows the enhanced contrast achievable after spectral integration between 4254  
 912 and 4333 nm, which also improves detection of complex wave patterns in several MAJIS  
 913 observations, like in C1 (panel c) and C13 (panel d). Pixel scales are reported in Table 1.

914

915 Following the discussion in Section 3.4, in Figure 20 we show the effect of the increased  
 916 contrast that can be achieved through the spectral integration of the CO<sub>2</sub> emission (right  
 917 panel), with respect to the single wavelength investigation (left panel). The integration of  
 918 course reduces noise hence allowing enhanced accuracy in detecting the wave patterns.  
 919 Indeed, if the radiance integrated in the band is considered, the detectable relative intensity  
 920 drops from 1% to about 0.5%, which of course translates as an enhanced capability in  
 921 characterizing the vertical structure of the waves.

922

#### 923 4.3.1. Atmospheric waves properties

924

925 Examples of wavy structures identified in the MAJIS images at 4270 nm are provided in  
 926 Figure 20. The wave packets have characteristics different from one image to the other in  
 927 terms of orientations and horizontal wavelengths. In some cases, a curved wavefront is  
 928 observed (see Figure 20 B, C, D) as well as a superposition between different packets  
 929 (Figure 20 D).

930

931

ID	Latitude (deg)	Packet length (km)	Packet width (km)	Horizontal wvl (km)	Azimuth (deg)
C1	9-10	157.6	36.1	27±7	163
C2	10-14	155	135.2	20±6	160
C4	20.85	107.9	94.7	21±6	162



C5	17.7-18.4	154.1	159.1	16±5	33.5
C6	22.9	74.5	94.8		133
C7	23.4-25.5	84.5	73.8	15±6	155
C13	19-22	134.6	88.1	24±8	123
C16	25-27	174.5	131	28±11	119

932 **Table 5:** Summary of parameters calculated from MAJIS data analysis. Columns indicate: image  
933 cube, latitude (deg), packet length (km), packet width (km), horizontal wavelength (km), azimuth (deg,  
934 see Section 3.4.1), respectively.

935

936 The values obtained from the method described in Section 3.4.1 are provided in Table 5. In  
937 the observed waves, the measured wavelengths are in the range ~ 15-40 km, which can be  
938 considered as short wavelengths. Similar waves can be generated by several sources and  
939 are usually observed in the stratosphere. According to models, deep convection is the  
940 principal source of forcing (Fovell et al. 1992; Piani et al. 2000; Lane et al. 2001) and is also  
941 suggested to be responsible for circular wave fronts (alongside isolated thunderstorm  
942 events, e.g. as observed from the Midcourse Space Experiment, Dewan et al. 1998).  
943 Another source of gravity waves, related to wind flow over mountains, is orography (Fritts  
944 and Alexander 2003; Kim et al. 2003) Depending on the topography, this can generate  
945 waves with horizontal scales from a few to hundreds of kilometers (Nastrom and Fritts, 1992;  
946 Dornbrack et al. 2002; Eckermann et al. 2007). However, as the majority of MAJIS EGA  
947 observations occurred above open sea areas, a possible origin related to a thunderstorm  
948 seems to be more realistic.

949 For circular waves, we estimate the packets' properties and the time of occurrence of the  
950 related thunderstorms (see Section 3.4.1). We assume storms occurring at an altitude of 15  
951 km and consider cubes C7 and C4 as examples. The minimum/maximum radii and the  
952 wavelengths obtained from the images are respectively 35, 50 and 15 km (cube C7) and 20,  
953 110 and 20 km (cube C4). In both cases, the thunderstorm triggering events result to be  
954 occurring about 1 h before the respective observations. This is compatible with the NASA  
955 Worldview archive, where several thunderstorms have been registered over the areas  
956 observed by MAJIS at around 05:00 local time. In particular, the wave detection in MAJIS C4  
957 acquisition is located about 80 km far from the coastline, and no significant orographic  
958 features are present along the apparent direction of propagation. For this detection, the  
959 hypothesis of thunderstorm-generated waves is also strengthened by the intense electrical  
960 activity confirmed in D'Aversa et al. (this issue), where a lightning event has been detected in  
961 the visible range of MAJIS cube C1 through the identification of neutral atomic oxygen and  
962 nitrogen emission lines.

963

#### 964 4.4. Land features

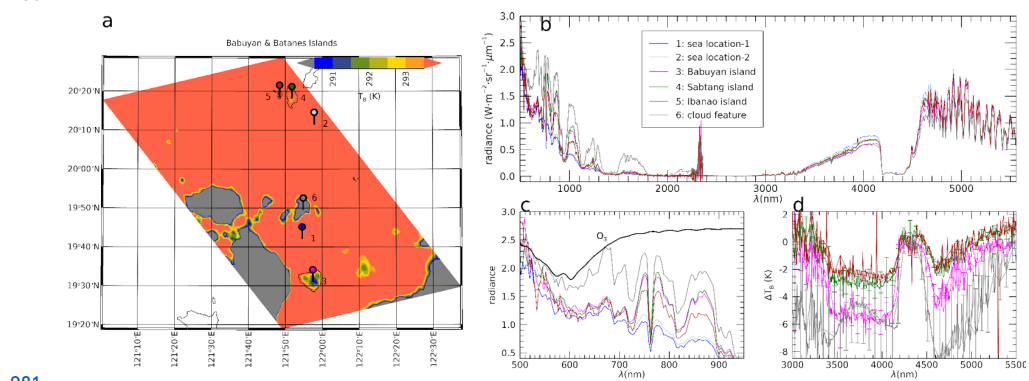
965

966 The land/ocean-contrast detection method described in Section 3.1 has been applied to all  
967 MAJIS cubes, but only a few land features have been identified. The C1 and C2 cubes,  
968 expected to cover large land areas at nighttime, encountered very thick and extended storm  
969 systems that prevented any surface visibility. Hence, all observable land regions consist of  
970 small islands seen in twilight illumination, colder than the surrounding sea surface but barely  
971 observable at visible wavelengths. Besides the largest example (Figure 7), other islands are



972 found in the cube C5 (Figure 21): Babuyan (region 3), Sabtang (region 4), and the very small  
973 Ibahos island (about  $4 \times 2.5$  km wide, region 5), all part of the Batanes archipelago. The  
974 nearby Dequey island, even smaller ( $\sim 0.7 \times 1$  km), remains unresolved. With respect to the  
975 ocean, the brightness temperatures measured over land and cloud areas (Figure 21b) are  
976 colder, with differences up to  $\sim 6$  K and  $\sim 8$  K respectively. Even if fully located beyond the  
977 terminator (solar incidence angle  $\sim 90.8^\circ$ ), a significant signal is detectable also at visible  
978 wavelengths, ascribable to light scattering in the upper illuminated portion of the atmospheric  
979 column, and to multiple scattering effects in the lower part.

980

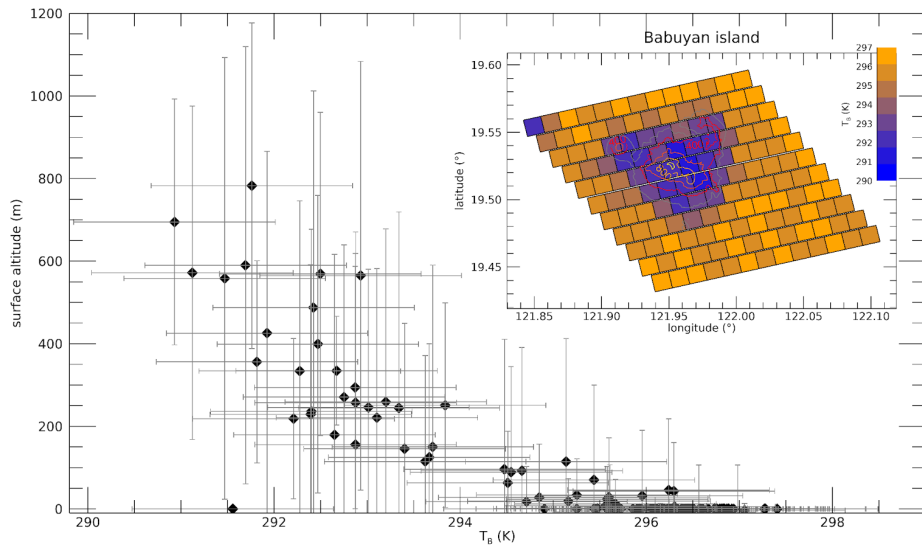


981

982 Figure 21: Land spectral features in the MAJIS cube C5. **a)** Brightness temperature map (at  
983 4610 nm) showing colder regions, identifiable as clouds (grey areas and region 6) and small  
984 islands: Babuyan (region 3), Sabtang (region 4) and Ibahos (region 5). Points labeled 1 and  
985 2 represent the locations for reference ocean spectra. **b)** MAJIS full-range spectra over the  
986 selected regions. **c)** Blow-up of the visible spectral part, showing  $H_2O$  and  $O_2$  absorption  
987 bands as well as a broad  $O_3$  absorption. **d)** Blow-up of the infrared spectral part given as  $T_B$   
988 difference with respect to the ocean spectrum. Coastlines data from OpenStreetMap,  
989 available under the Open Database License.

990

991 The MAJIS sensitivity to temperature variations can be estimated from the signal fluctuations  
992 over cloud-free ocean regions. The resulting uncertainties in thermal brightness (at 4610 nm)  
993 vary between 0.5 and 1 K, which correspond to about 0.2% and 0.4% of the spectral  
994 radiance at 293K. This sensitivity appears sufficient to discriminate significant temperature  
995 variation not only between sea and land surfaces but also between different land regions. As  
996 an example, we show in Figure 22 the variability of MAJIS brightness temperature inside the  
997 Babuyan island, which hosts a volcano of about 1 km in elevation (Babuyan Claro Volcano).  
998 Even if the spatial resolution is limited, a clear trend emerges with respect to the topographic  
999 altitude, suggesting that the MAJIS data are sensitive to the surface altimetric temperature  
1000 change.



1001

1002 **Figure 22:** Thermal analysis of Babuyan island, as viewed in MAJIS data cube C5. The  
 1003 MAJIS-derived brightness temperature (at 4610 nm) is plotted against topographic altitude,  
 1004 stressing the detection of surface altimetric temperature change. Error bars on the x axis are  
 1005 derived from signal fluctuation over sea surface around the island, while those on y axis  
 1006 represent the variability of surface altitude inside individual MAJIS pixels. Topographic data  
 1007 are extracted from Google Earth Pro 7.3.6.10441 (accessed Sep,03,2025).

1008

## 1009 5. Application to Jovian system science

1010

1011 This flyby represents the first acquisition of planetary data by MAJIS. Although the analysis  
 1012 presented here has been dedicated to Earth science, we can briefly identify and discuss  
 1013 different links to the MAJIS science that is foreseen at Jupiter and its icy satellites,  
 1014 highlighting the instrument capabilities in exploring different objects of the solar system.

1015

### 1016 5.1. From ice clouds to icy surfaces

1017

1018 The detection of terrestrial ice clouds described in Section 4.1 represents the first spectral  
 1019 observations of water ice performed by MAJIS, and is therefore the first approach to  
 1020 establish the potential outcomes from observations of Jovian icy satellites, in particular for  
 1021 Callisto and Ganymede.

1022 The investigation of ice properties possibly provides information on the differential evolution  
 1023 these bodies underwent in the Jovian system environment. For example, Callisto's surface is  
 1024 mainly covered by crystalline ice, while significant amorphous ice patches have been  
 1025 observed on Ganymede (e.g. Tosi et al., 2024, Bockelée-Morvan et al., 2024; Cartwright et  
 1026 al., 2024). These regions could indicate alteration through radiolysis induced by the  
 1027 impinging of charged particles on the ice (Khurana et al., 2007), hence providing information  
 1028 on the mechanisms connecting Jupiter's magnetic field lines and the moons' surfaces.  
 1029 Moreover, while Callisto is characterized by an overall low ice content on the surface (~  
 1030 50%) and presents a more ancient and stable scenario (Greeley et al., 2007), Ganymede's



1031 fresh ice patches are indicative of more frequent ice resurfacing and cryo-volcanism events  
1032 (Ligier et al., 2019). Smaller ice crystals are observed at the poles, matching the distribution  
1033 of the fresher ice deposits and hence acting as a tracer of geologic activity. In this view, the  
1034 investigation of ice-related spectral parameters can be used to address many scientific goals  
1035 of the JUICE mission (Stephan et al., 2021a; Poulet et al., 2024a).

1036

## 1037 5.2. *Clouds*

1038

1039 Jupiter's atmosphere is thought to be dominated by the presence of three main cloud decks  
1040 residing at different altitudes and mixed by convective processes and atmospheric circulation  
1041 (Fletcher et al., 2023). From lower to higher heights these are respectively composed of a  
1042  $H_2O-NH_3$  liquid solution,  $NH_4SH$  solid aggregates, and  $NH_3$  ice crystals (Atreya et al., 1999).  
1043 In particular, the  $NH_4SH$  and  $NH_3$  clouds can be responsible for the chromatic differences in  
1044 Jupiter's dark "belts" and bright "zones". Above these structures, hazes composed of  
1045 products of the photochemical disruption of  $CH_4$  and  $NH_3$  extend from the upper troposphere  
1046 to the stratosphere (e.g. Sindoni et al., 2017; Biagiotti et al., 2025). Such cloud complexity is  
1047 not present in Earth's atmosphere where water is the only condensable, aside from a variety  
1048 of aerosols of different origin (e.g. maritime, volcanic, smog, stratospheric). Nevertheless,  
1049 the study of EGA observations allows a first MAJIS data analysis devoted to disentangling  
1050 the spectral information related to different sources, like gases, clouds and, in this case, also  
1051 surfaces. In this manuscript we have investigated clouds under different points of view,  
1052 including their detection, water vapour phase identification, vertical structure assessment,  
1053 and microphysical properties estimation. All these techniques are applicable to Jupiter once  
1054 adapted to the different composition and structure of the giant planet. For example, the RT  
1055 modeling presented in Section 4.2.4 only dealt with the solar part of the spectrum, which  
1056 would only allow the investigation of Jupiter's hazes and the  $NH_3$  deck (e.g. the recent work  
1057 of Biagiotti et al., 2025 on JUNO/Jiram data). The exploitation of the full MAJIS spectral  
1058 range, including thermal wavelengths, is instead mandatory for characterizing the deeper  
1059  $NH_4SH$  (Grassi et al., 2021) and  $H_2O$  (Bjoraker et al., 2022) clouds, especially in "hot spot"  
1060 regions.

1061 The shadow technique for measuring cloud heights, commonly applied in planetary  
1062 high-resolution imaging analysis, is also applicable to Jupiter (e.g. Orton et al., 2017). For  
1063 instance, in observations acquired at the bottom of methane bands, Simon et al. (2015) were  
1064 able to measure shadows 45 km long, revealing wavy structures less than 1 km in amplitude.  
1065 In principle, MAJIS observations of Jupiter atmosphere will allow the application of this  
1066 technique to limited cases, mostly near the terminator and in polar regions when observed  
1067 from perijove. Maximum spatial resolutions of  $\sim 120$  km/px achievable in these conditions  
1068 may enable detecting shadows related to vertical displacements of the order of 10 km.

1069

1070

## 1071 5.3. *High-altitude emissions*

1072

1073 The use of chemical atmospheric species as tracers for the atmospheric circulation,  
1074 including wind measurements and wave detections, is widely applied to the investigation of  
1075 both terrestrial (i.e. Hueso et al. 2008; Peralta et al. 2008) and giant planets (i.e.  
1076 Müller-Wodarg et al. 2019, Grassi et al., 2020). A similar approach is valid for the upcoming  
1077 MAJIS measurements at the Jovian system, whose upper atmospheric dynamical structure  
1078 can be investigated through the monitoring of the distribution (in latitude and local time) of



1079 minor widespread species like  $\text{H}_3^+$  and hydrocarbons deriving from the photolysis of methane  
1080 (see Miller et al. 2020 for a thorough review) as demonstrated from both ground-based (see  
1081 for example O'Donoghue et al. 2016) and space-based data analyses (e.g. Moriconi et al.  
1082 2020). MAJIS IR channel will allow to spectrally discriminate the  $\text{CH}_4$  and  $\text{H}_3^+$  contributions in  
1083 the range 3000 - 4000 nm, where the two species present strong features (Castagnoli et al.,  
1084 2025) identifiable within the fundamental 3300 nm  $\text{CH}_4$  absorption band, similarly to the case  
1085 of the 4300 nm  $\text{CO}_2$  band in Earth's atmosphere (see Section 4.3). The study of  $\text{CH}_4$  and  $\text{H}_3^+$   
1086 (e.g. JWST data analysis, Melin et al., 2024) will give access to upper atmospheric layers  
1087 which are hardly probed otherwise. Altitudes from about 200 km above the 1-bar level are  
1088 typical of methane emission peak, while above 500 km the  $\text{H}_3^+$  emission seems to dominate,  
1089 as also shown by recent analyses of JIRAM-Juno data (Migliorini et al. 2023), where the two  
1090 species have been spatially separated.

1091

## 1092 6. Summary and conclusions

1093

1094 In this work we compare the observations of the MAJIS spectrometer on board the JUICE  
1095 spacecraft, acquired during the Earth gravity assist of 2024 (Section 1), with those registered  
1096 by the Italian Space Agency-led PRISMA spectrometer (Section 2). While no exact  
1097 temporal-spatial coincidence could be achieved, the comparison allowed testing MAJIS  
1098 spectral and radiometric response over ocean and clouds, the main targets observed during  
1099 this flyby. Clouds observations have been analyzed for the estimation of altitudes and  
1100 microphysical properties exploiting different methods (Section 4.2). Ice has been detected in  
1101 most of the observations, allowing a first benchmark of the study of its spectral properties  
1102 (Section 4.1) in view of Jupiter's icy satellites exploration.

1103 High-altitude emissions from  $\text{CO}_2$  and  $\text{O}_3$  are also observed in MAJIS dataset, revealing the  
1104 presence of a significant number of atmospheric gravity waves, whose properties have been  
1105 derived (Section 4.3).

1106 While we discuss *ad hoc* spectral indices for the identification at VIS-NIR wavelengths of  
1107 different types of surfaces (in view of the next JUICE Earth flyby happening in September  
1108 2026) our investigation of land features is limited to the land/ocean temperature contrast or  
1109 to the changing surface altimetry (Section 4.4). Indeed, in the MAJIS 2024 EGA data no land  
1110 areas have been captured in daylight.

1111 This wide variety of scientific applications is finally put in the context of the Jupiter case,  
1112 taking into account the differences between our planet and the gaseous giant's atmosphere  
1113 and icy satellites (Section 5).

1114 In conclusion, EGA data provide the first scientific benchmark of MAJIS instrumental  
1115 response in a planetary environment, and give the first glimpse of the amount and quality of  
1116 spectral information we can expect in the Jovian system.

1117

## 1118 Author Contributions

1119 Conceptualization, F.O., E.D., A.Mi.; formal analysis, F.O., E.D., A.Mi.; Data Curation, F.O.,  
1120 E.D., A.Mi., F.P., Y.L., G.P., A.Z., M.G., E.L., G.S., C.P., S.R., B.S.; investigation, F.O., E.D.,  
1121 A.Mi.; methodology, F.O., E.D., A.Mi.; software, F.O., E.D., A.Mi.; supervision, F.O., E.D.,  
1122 A.Mi., G.P., F.P., Y.L., G.F., M.C., M.R., B.S., A.M., L.N.F., A.Z., M.G., E.L., G.S., C.P.;  
1123 validation, F.O., E.D., A.Mi.; writing—original draft, F.O., E.D., A.Mi.; writing—review &  
1124 editing, F.O., E.D., A.Mi., G.P., F.P., L.N.F., A.M.. All authors have read and agreed to this  
1125 version of the manuscript.



**1126 Code availability**

**1127** The codes used in this manuscript have been developed by the authors and are available on  
**1128** request.

**1129 Competing interests**

**1130** The authors declare no competing interests in the production of this manuscript.

**1131**

**1132 Acknowledgements & Data availability**

**1133**

**1134** JUICE is a mission under ESA leadership with contributions from its Member States, NASA,  
**1135** JAXA and the Israel Space Agency. It is the first Large-class mission in ESA's Cosmic Vision  
**1136** programme. The Italian participation in the JUICE mission is funded by the Italian Space  
**1137** Agency (ASI). In particular, this work has been developed under the ASI-INAF agreement n.  
**1138** 2023-6-HH.0.

**1139** The MAJIS data acquired during the JUICE Moon–Earth flyby in August 2024 are currently  
**1140** under the mission's cruise-phase proprietary period. These data will be made available  
**1141** through the ESA Planetary Science Archive following the first Cruise Archive Delivery, which  
**1142** is currently scheduled for six months after Earth Gravity Assist #3 in 2029.

**1143** PRISMA products are generated by IAPS-INAF under a license from ASI Original PRISMA  
**1144** Product - © Italian Space Agency (ASI) – 2024. ASI retains copyright on the ORIGINAL  
**1145** Product "PRISMA Product - © Italian Space Agency (ASI) 2024. All rights reserved".

**1146**

**1147 References**

**1148**

**1149** Acton, C.H., 1996. Ancillary data services of NASA's navigation and ancillary infor-  
**1150** mation facility. *Planet. Space Sci.* 44 (1), 65–70.

**1151**

**1152** Acton, C., Bachman, N., Semenov, B., & Wright, E. (2018). A look towards the future  
**1153** in the handling of space science mission geometry. *Planetary and Space Science*,  
**1154** 150, 9–12. <https://doi.org/10.1016/j.pss.2017.02.013>

**1155**

**1156** Alexander, M. J., and J. R. Holton. "A Model Study of Zonal Forcing in the Equatorial  
**1157** Stratosphere by Convectively Induced Gravity Waves." *Journal of the Atmospheric*  
**1158** *Sciences* 54, no. 3 (1997): 408 - 419.

**1159** [https://doi.org/10.1175/1520-0469\(1997\)054<0408:amsozf>2.0.co;2](https://doi.org/10.1175/1520-0469(1997)054<0408:amsozf>2.0.co;2).

**1160**

**1161** Alexander, M. Joan, and Christopher Barnet. "Using Satellite Observations to  
**1162** Constrain Parameterizations of Gravity Wave Effects for Global Models." *Journal of*  
**1163** *the Atmospheric Sciences* 64, no. 5 (2007): 1652 - 1665.

**1164** <https://doi.org/10.1175/jas3897.1>.

**1165**

**1166** Atreya, S.K., M.H. Wong, T.C. Owen, et al. "A Comparison of the Atmospheres of



1167 Jupiter and Saturn: Deep Atmospheric Composition, Cloud Structure, Vertical Mixing,  
1168 and Origin." *Planetary and Space Science* 47, nos. 10–11 (1999): 1243 - 1262.  
1169 [https://doi.org/10.1016/s0032-0633\(99\)00047-1](https://doi.org/10.1016/s0032-0633(99)00047-1).

1170  
1171 Baldridge, A.M., S.J. Hook, C.I. Grove, and G. Rivera. "The ASTER Spectral Library  
1172 Version 2.0." *Remote Sensing of Environment* 113, no. 4 (2009): 711 - 715.  
1173 <https://doi.org/10.1016/j.rse.2008.11.007>.

1174  
1175 Baran, Anthony J. "A Review of the Light Scattering Properties of Cirrus." *Journal of*  
1176 *Quantitative Spectroscopy and Radiative Transfer* 110, nos. 14–16 (2009): 1239 -  
1177 1260. <https://doi.org/10.1016/j.jqsrt.2009.02.026>.

1178  
1179 Bekki, S., and F. Lefevre. "Stratospheric Ozone: History and Concepts and  
1180 Interactions with Climate." *The European Physical Journal Conferences* 1 (2009): 113  
1181 - 136. <https://doi.org/10.1140/epjconf/e2009-00914-y>.

1182  
1183 Berk, A., Conforti, P., Kennett, R., Perkins, T., Hawes, F., & van den Bosch, J. (2014).  
1184 *MODTRAN6: a major upgrade of the MODTRAN radiative transfer code*. Proc. SPIE  
1185 9088, Algorithms and Technologies for Multispectral, Hyperspectral, and Ultraspectral  
1186 Imagery XX, 90880H. doi:10.1117/12.2050433.

1187  
1188 Biagiotti, F, D Grassi, G Liuzzi, et al. "Evidence of Pure Ammonia Clouds in Jupiter's  
1189 Northern Temperate Domain from Juno/JIRAM Infrared Spectral Data." *Monthly*  
1190 *Notices of the Royal Astronomical Society* 538, no. 3 (2025): 1535 - 1564.  
1191 <https://doi.org/10.1093/mnras/staf381>.

1192  
1193 Bjoraker, Gordon L., Michael H. Wong, Imke de Pater, Tilak Hewagama, and Máté  
1194 Ádámkovics. "The Spatial Variation of Water Clouds, NH<sub>3</sub>, and H<sub>2</sub>O on Jupiter Using  
1195 Keck Data at 5 Microns." *Remote Sensing* 14, no. 18 (2022): 4567.  
1196 <https://doi.org/10.3390/rs14184567>.

1197  
1198 Bockelée-Morvan, D., et al., 2024. Composition and thermal properties of  
1199 Ganymede's surface from JWST/NIRSpec and MIRI observations. *A&A*, 681.

1200  
1201 Bovensmann, H., J. P. Burrows, M. Buchwitz, et al. "SCIAMACHY: Mission  
1202 Objectives and Measurement Modes." *Journal of the Atmospheric Sciences* 56, no. 2  
1203 (1999): 127 - 150.



1204 [https://doi.org/10.1175/1520-0469\(1999\)056<0127:smoamm>2.0.co;2](https://doi.org/10.1175/1520-0469(1999)056<0127:smoamm>2.0.co;2).

1205

1206 Butz, A., S. Guerlet, O. Hasekamp, et al. "Toward Accurate CO<sub>2</sub> and CH<sub>4</sub>  
1207 Observations from GOSAT." *Geophysical Research Letters* 38, no. 14 (2011).  
1208 <https://doi.org/10.1029/2011gl047888>.

1209

1210 Cartwright, Richard J., Charles A. Hibbitts, Bryan J. Holler, et al. "Jwst Reveals  
1211 Spectral Tracers of Recent Surface Modification on Europa." *The Planetary Science  
1212 Journal* 6, no. 5 (2025): 125. <https://doi.org/10.3847/psj/adcab9>.

1213

1214 Cartwright, R.J., et al., 2025. Revealing Callisto's Carbon-rich Surface and CO<sub>2</sub>  
1215 Atmosphere with JWST. *Planetary Science Journal*, 5, 60.

1216

1217 Cassini, Lorenzo, Guido Masiello, Sergio De Souza-Machado, Manuel  
1218 López-Puertas, Larrabee Strow, Giuliano Liuzzi, Christopher Hepplewhite, Tiziano  
1219 Maestri, Michele Martinazzo, Carmine Serio, "Updates to 4.3um CO<sub>2</sub> NLTE modeling  
1220 for nadir hyperspectral infrared sounders," Proc. SPIE 13668, Remote Sensing of  
1221 Clouds and the Atmosphere XXX, 1366809 (29 October 2025);  
1222 <https://doi.org/10.1117/12.3069902>

1223

1224 Castagnoli, Chiara, Bianca M. Dinelli, Francesca Altieri, et al. "Characterization and  
1225 Sensitivity Analysis of JIRAM Spectra for Optimizing CH<sub>4</sub> and H<sub>3</sub>+ Retrieval." *The  
1226 Planetary Science Journal* 6, no. 4 (2025): 93. <https://doi.org/10.3847/psj/adbf8>.

1227

1228 Clark, Roger N., Dale P. Cruikshank, Ralf Jaumann, et al. "The Surface Composition  
1229 of Iapetus: Mapping Results from Cassini VIMS." *Icarus* 218, no. 2 (2012): 831 - 860.  
1230 <https://doi.org/10.1016/j.icarus.2012.01.008>.

1231

1232 Coradini, A., F. Capaccioni, P. Drossart, A. Semery, G. Arnold, and U. Schade.  
1233 "VIRTIS: The Imaging Spectrometer of the Rosetta Mission." *Advances in Space  
1234 Research* 24, no. 9 (1999): 1095 - 1104.  
1235 [https://doi.org/10.1016/s0273-1177\(99\)80203-8](https://doi.org/10.1016/s0273-1177(99)80203-8).

1236

1237 D'Aversa, Emiliano, Fabrizio Oliva, Francesca Altieri, et al. "Vertical Distribution of  
1238 Dust in the Martian Atmosphere: OMEGA/MEx Limb Observations." *Icarus* 371  
1239 (January 2022): 114702. <https://doi.org/10.1016/j.icarus.2021.114702>.

1240



1241 D'Aversa, E., et al.: Spectroscopic detection of terrestrial lightning from space by  
1242 JUICE-MAJIS during Earth Gravity Assist, *Ann. Geophys.*, submitted to this issue.

1243  
1244 Dewan, E. M., and R. E. Good. "Saturation and the 'Universal' Spectrum for Vertical  
1245 Profiles of Horizontal Scalar Winds in the Atmosphere." *Journal of Geophysical*  
1246 *Research: Atmospheres* 91, no. D2 (1986): 2742 - 2748.  
1247 <https://doi.org/10.1029/jd091id02p02742>.

1248  
1249 Dewan, E. M., R. H. Picard, R. R. O'Neil, et al. "MSX Satellite Observations of  
1250 Thunderstorm-generated Gravity Waves in Mid-wave Infrared Images of the Upper  
1251 Stratosphere." *Geophysical Research Letters* 25, no. 7 (1998): 939 - 942.  
1252 <https://doi.org/10.1029/98gl00640>.

1253  
1254 Dolan, Brenda, Pavlos Kollias, Susan C. van den Heever, et al. "Time Resolved  
1255 Reflectivity Measurements of Convective Clouds." *Geophysical Research Letters* 50,  
1256 no. 22 (2023). <https://doi.org/10.1029/2023gl105723>.

1257  
1258 Dörnbrack, Andreas, Thomas Birner, Andreas Fix, et al. "Evidence for Inertia Gravity  
1259 Waves Forming Polar Stratospheric Clouds over Scandinavia." *Journal of*  
1260 *Geophysical Research: Atmospheres* 107, no. D20 (2002).  
1261 <https://doi.org/10.1029/2001jd000452>.

1262  
1263 Drossart, Pierre, Giuseppe Piccioni, Angioletta Coradini, et al. "VIRTIS Imaging  
1264 Spectrometer for the ESA/Venus Express Mission." *SPIE Proceedings* 5543  
1265 (November 2004): 175. <https://doi.org/10.1117/12.557427>.

1266  
1267 Eckermann, Stephen D., Jun Ma, Dong L. Wu, and Dave Broutman. "A  
1268 Three-dimensional Mountain Wave Imaged in Satellite Radiance throughout the  
1269 Stratosphere: Evidence of the Effects of Directional Wind Shear." *Quarterly Journal of*  
1270 *the Royal Meteorological Society* 133, no. 629 (2007): 1959 - 1975.  
1271 <https://doi.org/10.1002/qj.187>.

1272  
1273 Efremenko, Dmitry, and Alexander Kokhanovsky. *Foundations of Atmospheric*  
1274 *Remote Sensing*. Springer Nature, 2021.

1275  
1276 Ehrlich, A., E. Bierwirth, M. Wendisch, et al. "Cloud Phase Identification of Arctic



1277        Boundary-Layer Clouds from Airborne Spectral Reflection Measurements: Test of  
1278        Three Approaches." *Atmospheric Chemistry and Physics* 8, no. 24 (2008): 7493 -  
1279        7505. <https://doi.org/10.5194/acp-8-7493-2008>.

1280  
1281        Eldering, Annmarie, Thomas E. Taylor, Christopher W. O'Dell, and Ryan Pavlick.  
1282        "The OCO-3 Mission: Measurement Objectives and Expected Performance Based on  
1283        1 Year of Simulated Data." *Atmospheric Measurement Techniques* 12, no. 4 (2019):  
1284        2341 - 2370. <https://doi.org/10.5194/amt-12-2341-2019>.

1285  
1286        Filacchione, Gianrico, Emiliano D'Aversa, Fabrizio Capaccioni, et al. "Saturn's Icy  
1287        Satellites Investigated by Cassini-VIMS. IV. Daytime Temperature Maps." *Icarus* 271  
1288        (June 2016): 292 - 313. <https://doi.org/10.1016/j.icarus.2016.02.019>.

1289  
1290        Filacchione, G., Capaccioni, F., Ciarniello, M., et al., 2012. Saturn's icy satellites and  
1291        rings investigated by cassini-VIMS: III—Radial compositional variability. *Icarus*  
1292        220, 1064–1096.

1293  
1294        Fink, Uwe, and Harold P. Larson. "Temperature Dependence of the Water-Ice  
1295        Spectrum between 1 and 4 Microns: Application to Europa, Ganymede and Saturn's  
1296        Rings." *Icarus* 24, no. 4 (1975): 411 - 420.  
1297        [https://doi.org/10.1016/0019-1035\(75\)90058-5](https://doi.org/10.1016/0019-1035(75)90058-5).

1298  
1299        Fletcher, L.N., et al., 2023. Jupiter Science Enabled by ESA's Jupiter Icy Moons  
1300        Explorer. *Space Science Review*, vol. 219, n. 53, 2023.

1301  
1302        Fovell, R., D. Durran, and J. R. Holton. "Numerical Simulations of Convectively  
1303        Generated Stratospheric Gravity Waves." *Journal of the Atmospheric Sciences* 49,  
1304        no. 16 (1992): 1427 - 1442.  
1305        [https://doi.org/10.1175/1520-0469\(1992\)049<1427:nsocgs>2.0.co;2](https://doi.org/10.1175/1520-0469(1992)049<1427:nsocgs>2.0.co;2).

1306  
1307        Fritts, David C., and M. Joan Alexander. "Gravity Wave Dynamics and Effects in the  
1308        Middle Atmosphere." *Reviews of Geophysics* 41, no. 1 (2003).  
1309        <https://doi.org/10.1029/2001rg000106>.

1310  
1311        Fu, Dongwei, Larry Di Girolamo, Robert M. Rauber, et al. "An Evaluation of the Liquid  
1312        Cloud Droplet Effective Radius Derived from MODIS, Airborne Remote Sensing, and  
1313        in Situ Measurements from CAMP2Ex." *Atmospheric Chemistry and Physics* 22, no.



1314 12 (2022): 8259 - 8285. <https://doi.org/10.5194/acp-22-8259-2022>.

1315

1316 Geddes, A., and H. Bösch. "Tropospheric Aerosol Profile Information from  
1317 High-Resolution Oxygen A-Band Measurements from Space." *Atmospheric  
1318 Measurement Techniques* 8, no. 2 (2015): 859 - 874.  
1319 <https://doi.org/10.5194/amt-8-859-2015>.

1320

1321 Gordon, I.E., L.S. Rothman, R.J. Hargreaves, et al. "The HITRAN2020 Molecular  
1322 Spectroscopic Database." *Journal of Quantitative Spectroscopy and Radiative  
1323 Transfer* 277 (January 2022): 107949. <https://doi.org/10.1016/j.jqsrt.2021.107949>.

1324

1325 Gorshelev, V., A. Serdyuchenko, M. Weber, W. Chehade, and J. P. Burrows. "High  
1326 Spectral Resolution Ozone Absorption Cross-Sections – Part 1: Measurements, Data  
1327 Analysis and Comparison with Previous Measurements around 293 K." *Atmospheric  
1328 Measurement Techniques* 7, no. 2 (2014): 609 - 624.  
1329 <https://doi.org/10.5194/amt-7-609-2014>.

1330

1331 Gorshelev, V., A. Serdyuchenko, M. Weber, W. Chehade, and J. P. Burrows. "High  
1332 Spectral Resolution Ozone Absorption Cross-Sections – Part 1: Measurements, Data  
1333 Analysis and Comparison with Previous Measurements around 293 K." *Atmospheric  
1334 Measurement Techniques* 7, no. 2 (2014): 609 - 624.  
1335 <https://doi.org/10.5194/amt-7-609-2014>.

1336

1337 Grassi, Davide, A Mura, G Sindoni, et al. "On the Clouds and Ammonia in Jupiter's  
1338 Upper Troposphere from Juno JIRAM Reflectivity Observations." *Monthly Notices of  
1339 the Royal Astronomical Society* 503, no. 4 (2021): 4892 - 4907.  
1340 <https://doi.org/10.1093/mnras/stab740>.

1341

1342 Grassi, D., et al., 2020. On the Spatial Distribution of Minor Species in Jupiter's  
1343 Troposphere as Inferred From Juno JIRAM Data. *JGR Planets*, 125, 4.

1344

1345 Greeley, R., C.F. Chyba, J.W. Head III, W.B. McKinnon, R.T. Pappalardo, and P.H.  
1346 Figueredo. "The Geology of Europa." In *Jupiter: The Planet, Satellites and  
1347 Magnetosphere*, edited by F. Bagenal, T. Dowling, and W. McKinnon. Cambridge  
1348 University Press, 2007.

1349

1350 Grundy, W. M., and B. Schmitt. "The Temperature-dependent Near-infrared



1351        Absorption Spectrum of Hexagonal H<sub>2</sub>O Ice." *Journal of Geophysical Research: Planets* 103, no. E11 (1998): 25809 - 25822. <https://doi.org/10.1029/98je00738>.

1353

1354        Haffoud, Paolo, François Poulet, Mathieu Vincendon, et al. "Calibration of MAJIS (Moons And Jupiter Imaging Spectrometer). III. Spectral Calibration." *Review of Scientific Instruments* 95, no. 3 (2024). <https://doi.org/10.1063/5.0188944>.

1355

1356

1357

1358        Hale, George M., and Marvin R. Querry. "Optical Constants of Water in the 200 Nm to 200 Mm Wavelength Region." *Applied Optics* 12, no. 3 (1973): 555.

1359

1360        <https://doi.org/10.1364/ao.12.000555>.

1361

1362        Hamilton, Kevin. "Comprehensive Meteorological Modelling of the Middle Atmosphere: A Tutorial Review." *Journal of Atmospheric and Terrestrial Physics* 58, no. 14 (1996): 1591 - 1627. [https://doi.org/10.1016/0021-9169\(96\)00028-1](https://doi.org/10.1016/0021-9169(96)00028-1).

1363

1364

1365

1366        Heintzenberg, J., D. C. Covert, and R. Van Dingenen. "Size Distribution and Chemical Composition of Marine Aerosols: A Compilation and Review." *Tellus B: Chemical and Physical Meteorology* 52, no. 4 (2000): 1104.

1367

1368

1369        <https://doi.org/10.3402/tellusb.v52i4.17090>.

1370

1371        Hines, C. O. "Internal Atmospheric Gravity Waves at Ionospheric Heights." *Canadian Journal of Physics* 38, no. 11 (1960): 1441 - 1481. <https://doi.org/10.1139/p60-150>.

1372

1373

1374        Hueso, R., A. Sánchez-Lavega, G. Piccioni, et al. "Morphology and Dynamics of Venus Oxygen Airglow from Venus Express/Visible and Infrared Thermal Imaging Spectrometer Observations." *Journal of Geophysical Research: Planets* 113, no. E5 (2008). <https://doi.org/10.1029/2008je003081>.

1375

1376

1377

1378

1379        Hurley, J., P.G.J. Irwin, A. Adriani, et al. "Analysis of Rosetta/VIRTIS Spectra of Earth Using Observations from ENVISAT/AATSR, TERRA/MODIS and ENVISAT/SCIAMACHY, and Radiative-Transfer Simulations." *Planetary and Space Science* 90 (January 2014): 37 - 59. <https://doi.org/10.1016/j.pss.2013.06.012>.

1380

1381

1382

1383

1384        Kim, Young-Joon, Stephen D. Eckermann, and Hye-Yeong Chun. "An Overview of the Past, Present and Future of Gravity-wave Drag Parametrization for Numerical Climate and Weather Prediction Models." *Atmosphere-Ocean* 41, no. 1 (2003): 65 - 98. <https://doi.org/10.3137/ao.410105>.

1385

1386

1387



1388  
1389 Kitamura, Rei, Laurent Pilon, and Miroslaw Jonasz. "Optical Constants of Silica Glass  
1390 from Extreme Ultraviolet to Far Infrared at near Room Temperature." *Applied Optics*  
1391 46, no. 33 (2007): 8118. <https://doi.org/10.1364/ao.46.008118>.

1392  
1393 Krisna, Trismono C., Manfred Wendisch, André Ehrlich, et al. "Comparing Airborne  
1394 and Satellite Retrievals of Cloud Optical Thickness and Particle Effective Radius  
1395 Using a Spectral Radiance Ratio Technique: Two Case Studies for Cirrus and Deep  
1396 Convective Clouds." *Atmospheric Chemistry and Physics* 18, no. 7 (2018): 4439 -  
1397 4462. <https://doi.org/10.5194/acp-18-4439-2018>.

1398  
1399 Kuang, Zhiming, Jack Margolis, Geoffrey Toon, David Crisp, and Yuk Yung.  
1400 "Spaceborne Measurements of Atmospheric CO<sub>2</sub> by High-resolution NIR  
1401 Spectrometry of Reflected Sunlight: An Introductory Study." *Geophysical Research  
1402 Letters* 29, no. 15 (2002). <https://doi.org/10.1029/2001gl014298>.

1403  
1404 Khurana, K.K., et al., 2007. The origin of Ganymedes' polar caps. *Icarus*, 191, 1,  
1405 193-202. <https://doi.org/10.1016/j.icarus.2007.04.022>

1406  
1407 Langevin, Y., F. Poulet, G. Piccioni, et al. "Calibration of MAJIS (Moons and Jupiter  
1408 Imaging Spectrometer). IV. Radiometric Calibration (Invited)." *Review of Scientific  
1409 Instruments* 95, no. 11 (2024). <https://doi.org/10.1063/5.0202702>.

1410  
1411  
1412 Langevin, Y., Rodriguez, S., Poulet, F., Guerlet, S., Armante, R., Agostini, L.,  
1413 D'Aversa, E., Royer, C., Fletcher, L., Oliva, F., Seignovert, B., Stephan, K., and Tosi,  
1414 F.: Post-launch spectral and radiometric performances of MAJIS, the VIS–NIR  
1415 imaging spectrometer of JUICE, *Ann. Geophys.*, submitted to this issue.

1416  
1417 LeMone, Margaret A. "International Cloud Atlas: Manual on the Observation of  
1418 Clouds and Other Meteors." In *International Cloud Atlas*. World Meteorological  
1419 Organization, 1988.

1420  
1421 Ligier, N., C. Paranicas, J. Carter, et al. "Surface Composition and Properties of  
1422 Ganymede: Updates from Ground-Based Observations with the near-Infrared  
1423 Imaging Spectrometer SINFONI/VLT/ESO." *Icarus* 333 (November 2019): 496 - 515.



1424 <https://doi.org/10.1016/j.icarus.2019.06.013>.

1425

1426 *Ettore Lopinto, Luca Fasano, Francesco Longo, Giancarlo Varacalli, Patrizia Sacco, Leandro Chiarantini, Francesco Sarti, Luigi Agrimano, Francesca Santoro, Sergio Cogliati, Roberto Colombo, Mariano Bresciani, Claudia Giardino, Federica Braga*

1427 Current Status and Future Perspectives of the PRISMA Mission at the Turn of One

1428 Year in Operational Usage 2021 IEEE International Geoscience and Remote Sensing

1429 Symposium IGARSS <https://doi.org/10.1109/IGARSS47720.2021.9553301>

1430

1431

1432

1433 Luo, Tao, Renmin Yuan, and Zhien Wang. "On Factors Controlling Marine Boundary

1434 Layer Aerosol Optical Depth." *Journal of Geophysical Research: Atmospheres* 119,

1435 no. 6 (2014): 3321 - 3334. <https://doi.org/10.1002/2013jd020936>.

1436

1437 Mastrapa, R, M Bernstein, S Sandford, T Roush, D Cruikshank, and C Ore. "Optical

1438 Constants of Amorphous and Crystalline H<sub>2</sub>O Ice in the near Infrared from 1.1 to 2.6

1439 \$μm." *Icarus* 197, no. 1 (2008): 307 - 320.

1440 <https://doi.org/10.1016/j.icarus.2008.04.008>.

1441

1442 Mastrapa, R. M., S. A. Sandford, T. L. Roush, D. P. Cruikshank, and C. M. Dalle Ore.

1443 "Optical Constant of Amorphous and Crystalline H<sub>2</sub>O Ice: 2.5-22 Mm (4000-455

1444 Cm-1) Otpical Constants of H<sub>2</sub>O Ice." *The Astrophysical Journal* 701, no. 2 (2009):

1445 1347 - 1356. <https://doi.org/10.1088/0004-637x/701/2/1347>.

1446

1447 Melin, H., O'Donoghue, J., Moore, L., Stallard, T. S., Fletcher, L. N., Roman, M. T.,

1448 Harkett, J., King, O. R. T., Thomas, E. M., Wang, R., Tiranti, P. I., Knowles, K. L., de

1449 Pater, I., Fouchet, T., Fry, P. H., Wong, M. H., Holler, B. J., Hueso, R., James, M. K.,

1450 ... Showalter, M. R. (2024). Ionospheric irregularities at Jupiter observed by JWST.

1451 *Nature Astronomy*, 8(8), 1000–1007. <https://doi.org/10.1038/s41550-024-02305-9>.

1452

1453 Migliorini, A., B. M. Dinelli, C. Castagnoli, et al. "First Observations of CH<sub>4</sub> and

1454 Spatially Resolved Emission Layers at Jupiter Equator, as Seen by JIRAM/Juno."

1455 *Journal of Geophysical Research: Planets* 128, no. 3 (2023).

1456 <https://doi.org/10.1029/2022je007509>.

1457



1458 Miller, Steve, Jonathan Tennyson, Thomas R. Geballe, and Tom Stallard. "Thirty  
1459 Years of H3+ Astronomy." *Reviews of Modern Physics* 92, no. 3 (2020).  
1460 <https://doi.org/10.1103/revmodphys.92.035003>.

1461  
1462 Moriconi, M. L., A. Migliorini, F. Altieri, et al. "Turbulence Power Spectra in Regions  
1463 Surrounding Jupiter's South Polar Cyclones from Juno/JIRAM." *Journal of  
1464 Geophysical Research: Planets* 125, no. 7 (2020).  
1465 <https://doi.org/10.1029/2019je006096>.

1466  
1467 Müller-Wodarg, I. C. F., T. T. Koskinen, L. Moore, et al. "Atmospheric Waves and  
1468 Their Possible Effect on the Thermal Structure of Saturn's Thermosphere."  
1469 *Geophysical Research Letters* 46, no. 5 (2019): 2372 - 2380.  
1470 <https://doi.org/10.1029/2018gl081124>.

1471  
1472 Nakajima, Takashi Y., Haruma Ishida, Takashi M. Nagao, et al. "Theoretical Basis of  
1473 the Algorithms and Early Phase Results of the GCOM-C (Shikisai) SGLI Cloud  
1474 Products." *Progress in Earth and Planetary Science* 6, no. 1 (2019).  
1475 <https://doi.org/10.1186/s40645-019-0295-9>.

1476  
1477 Nastrom, Gregory D., and David C. Fritts. "Sources of Mesoscale Variability of  
1478 Gravity Waves. Part i: Topographic Excitation." *Journal of the Atmospheric Sciences*  
1479 49, no. 2 (1992): 101 - 110.  
1480 [https://doi.org/10.1175/1520-0469\(1992\)049<0101:somvog>2.0.co;2](https://doi.org/10.1175/1520-0469(1992)049<0101:somvog>2.0.co;2).

1481  
1482 Newnham, David A., and John Ballard. "Visible Absorption Cross Sections and  
1483 Integrated Absorption Intensities of Molecular Oxygen (O2 and O4)." *Journal of  
1484 Geophysical Research: Atmospheres* 103, no. D22 (1998): 28801 - 28815.  
1485 <https://doi.org/10.1029/98jd02799>.

1486  
1487 O'Donoghue, J., L. Moore, T. S. Stallard, and H. Melin. "Heating of Jupiter's Upper  
1488 Atmosphere above the Great Red Spot." *Nature* 536, no. 7615 (2016): 190 - 192.  
1489 <https://doi.org/10.1038/nature18940>.

1490  
1491 Oliva, F., A. Adriani, M.L. Moriconi, G.L. Liberti, E. D'Aversa, and G. Filacchione.  
1492 "Clouds and Hazes Vertical Structure of a Saturn's Giant Vortex from Cassini/VIMS-V  
1493 Data Analysis." *Icarus* 278 (November 2016): 215 - 237.  
1494 <https://doi.org/10.1016/j.icarus.2016.06.021>.



1495  
1496 Oliva, F., A. Geminale, E. D'Aversa, et al. "Properties of a Martian Local Dust Storm  
1497 in Atlantis Chaos from OMEGA/MEX Data." *Icarus* 300 (January 2018): 1 - 11.  
1498 <https://doi.org/10.1016/j.icarus.2017.07.034>.

1499  
1500 Oliva, F., G. Piccioni, E. D'Aversa, et al. "Earth as an Exoplanet: VIRTIS-M/Venus  
1501 Express Data Analysis." *EPSC Abstracts* 11 (2017).

1502  
1503 Orton, G.S., et al., 2017. The first close-up images of Jupiter's polar regions: Results  
1504 from the Juno mission JunoCam instrument. *Geophysical Research Letters*, 44, 10,  
1505 4599-4606.

1506  
1507 Peralta, J., R. Hueso, A. Sánchez-Lavega, G. Piccioni, O. Lanciano, and P. Drossart.  
1508 "Characterization of Mesoscale Gravity Waves in the Upper and Lower Clouds of  
1509 Venus from VEX-VIRTIS Images." *Journal of Geophysical Research: Planets* 113, no.  
1510 E5 (2008). <https://doi.org/10.1029/2008je003185>.

1511  
1512 Piani, C., D. Durran, M. J. Alexander, and J. R. Holton. "A Numerical Study of  
1513 Three-Dimensional Gravity Waves Triggered by Deep Tropical Convection and Their  
1514 Role in the Dynamics of the QBO." *Journal of the Atmospheric Sciences* 57, no. 22  
1515 (2000): 3689 - 3702.  
1516 [https://doi.org/10.1175/1520-0469\(2000\)057<3689:ansotd>2.0.co;2](https://doi.org/10.1175/1520-0469(2000)057<3689:ansotd>2.0.co;2).

1517  
1518 Piccioni, Giuseppe, Alessandro Bini, Giulio Bugetti, et al. "Scientific Goals and  
1519 Technical Challenges of the MAJIS Imaging Spectrometer for the JUICE Mission."  
1520 *2019 IEEE 5th International Workshop on Metrology for AeroSpace*  
1521 (*MetroAeroSpace*), IEEE, June 2019, 318 - 323.  
1522 <https://doi.org/10.1109/metroaerospace.2019.8869566>.

1523  
1524 S. Pignatti *et al.*, "The PRISMA hyperspectral mission: Science activities and  
1525 opportunities for agriculture and land monitoring," *2013 IEEE International*  
1526 *Geoscience and Remote Sensing Symposium - IGARSS*, Melbourne, VIC, Australia,  
1527 2013, pp. 4558-4561, doi: 10.1109/IGARSS.2013.6723850.

1528  
1529 Poulet, F., G. Piccioni, Y. Langevin, et al. "Moons and Jupiter Imaging Spectrometer  
1530 (MAJIS) on Jupiter Icy Moons Explorer (JUICE)." *Space Science Reviews* 220, no. 3  
1531 (2024a). <https://doi.org/10.1007/s11214-024-01057-2>.



1532  
1533 Poulet, F., Piccioni, G., Langevin, Y., et al. *ESA/JUICE encounters Earth/Moon in*  
1534 *2024: overview of the Moons And Jupiter Imaging Spectrometer (MAJIS)*  
1535 *observations. Ann. Geophys.*, submitted to this issue

1536  
1537 Poulet, F., Langevin, Y., and Piccioni, G.: *Calibration of the Moons And Jupiter*  
1538 *Imaging Spectrometer (MAJIS): Introduction to the special collection and summary of*  
1539 *the performances, Rev. Sci. Instrum.*, 95, 071601, <https://doi.org/10.1063/5.0209679>,  
1540 2024b

1541  
1542 Rossow, William B., and Robert A. Schiffer. "Advances in Understanding Clouds from  
1543 *ISCCP.*" *Bulletin of the American Meteorological Society* 80, no. 11 (1999): 2261 -  
1544 2287. [https://doi.org/10.1175/1520-0477\(1999\)080<2261:aiucfi>2.0.co;2](https://doi.org/10.1175/1520-0477(1999)080<2261:aiucfi>2.0.co;2).

1545  
1546 Seignovert, B., Poulet, F., Langevin, Y., D'Aversa, E., Ligier, N., Mesbout, M., Leyrat,  
1547 C., Le Mouélic, S., Stephan, K., Palumbo, P., Agostini, L., Pensa, L., Le Deit, L.,  
1548 Cornet, T., Belgacem, I., Costa, M., and Escalante Lopez, A.: *MAJIS onboard*  
1549 *geometric calibration during 1320 the early cruise phase, Ann. Geophys.*, submitted  
1550 to this issue.

1551  
1552 Simon, A. A., L. Li, and D. C. Reuter. "Small-scale Waves on Jupiter: A Reanalysis of  
1553 *New Horizons, Voyager, and Galileo Data.*" *Geophysical Research Letters* 42, no. 8  
1554 (2015): 2612 - 2618. <https://doi.org/10.1002/2015gl063433>.

1555  
1556 Sindoni, G., D. Grassi, A. Adriani, et al. "Characterization of the White Ovals on  
1557 *Jupiter's Southern Hemisphere Using the First Data by the Juno/JIRAM Instrument.*"  
1558 *Geophysical Research Letters* 44, no. 10 (2017): 4660 - 4668.  
1559 <https://doi.org/10.1002/2017gl072940>.

1560  
1561 Smirnov, Alexander, Brent N. Holben, Yoram J. Kaufman, et al. "Optical Properties of  
1562 *Atmospheric Aerosol in Maritime Environments.*" *Journal of the Atmospheric*  
1563 *Sciences* 59, no. 3 (2002): 501 - 523.  
1564 [https://doi.org/10.1175/1520-0469\(2002\)059<0501:opoaaai>2.0.co;2](https://doi.org/10.1175/1520-0469(2002)059<0501:opoaaai>2.0.co;2).

1565  
1566 Smith, K.M, and D.A Newnham. "Near-Infrared Absorption Spectroscopy of Oxygen  
1567 *and Nitrogen Gas Mixtures.*" *Chemical Physics Letters* 308, nos. 1–2 (1999): 1 - 6.  
1568 [https://doi.org/10.1016/s0009-2614\(99\)00584-9](https://doi.org/10.1016/s0009-2614(99)00584-9).



1569  
1570 Stephan, Katrin, Mauro Ciarniello, Olivier Poch, Bernard Schmitt, David Haack, and  
1571 Andrea Raponi. "VIS-NIR/SWIR Spectral Properties of H<sub>2</sub>O Ice Depending on  
1572 Particle Size and Surface Temperature." *Minerals* 11, no. 12 (2021): 1328.  
1573 <https://doi.org/10.3390/min11121328>.

1574  
1575 Stephan, Katrin, T. Roatsch, F. Tosi, et al. "Regions of Interest on Ganymede's and  
1576 Callisto's Surfaces as Potential Targets for ESA's JUICE Mission." *Planetary and*  
1577 *Space Science* 208 (November 2021a): 105324.  
1578 <https://doi.org/10.1016/j.pss.2021.105324>.

1579  
1580 Stevens, Michael H., Christoph R. Englert, John M. Harlander, et al. "Retrieval of  
1581 Lower Thermospheric Temperatures from O<sub>2</sub> A Band Emission: The MIGHTI  
1582 Experiment on ICON." *Space Science Reviews* 214, no. 1 (2017).  
1583 <https://doi.org/10.1007/s11214-017-0434-9>.

1584  
1585 Sun, Kangwen, Guangyao Dai, Songhua Wu, et al. *Correlation between Marine*  
1586 *Aerosol Optical Properties and Wind Fields over Remote Oceans with Use of*  
1587 *Spaceborne Lidar Observations*. Copernicus GmbH, 2023.  
1588 <https://doi.org/10.5194/egusphere-2023-433>.

1589  
1590 Taylor, M.J., and M.A. Hapgood. "Identification of a Thunderstorm as a Source of  
1591 Short Period Gravity Waves in the Upper Atmospheric Nightglow Emissions."  
1592 *Planetary and Space Science* 36, no. 10 (1988): 975 - 985.  
1593 [https://doi.org/10.1016/0032-0633\(88\)90035-9](https://doi.org/10.1016/0032-0633(88)90035-9).

1594  
1595 Thomason, L. W., S. P. Burton, B.-P. Luo, and T. Peter. "SAGE II Measurements of  
1596 Stratospheric Aerosol Properties at Non-Volcanic Levels." *Atmospheric Chemistry*  
1597 *and Physics* 8, no. 4 (2008): 983 - 995. <https://doi.org/10.5194/acp-8-983-2008>.

1598  
1599 Tosi, Federico, Thomas Roatsch, André Galli, et al. "Characterization of the Surfaces  
1600 and Near-Surface Atmospheres of Ganymede, Europa and Callisto by JUICE."  
1601 *Space Science Reviews* 220, no. 5 (2024).  
1602 <https://doi.org/10.1007/s11214-024-01089-8>.

1603  
1604 van Diedenhoven, Bastiaan, Ann M. Fridlind, Brian Cairns, Andrew S. Ackerman, and  
1605 John E. Yorks. "Vertical Variation of Ice Particle Size in Convective Cloud Tops."



1606 *Geophysical Research Letters* 43, no. 9 (2016): 4586 - 4593.

1607 <https://doi.org/10.1002/2016gl068548>.

1608

1609 Veefkind, J.P., I. Aben, K. McMullan, et al. "TROPOMI on the ESA Sentinel-5

1610 Precursor: A GMES Mission for Global Observations of the Atmospheric Composition

1611 for Climate, Air Quality and Ozone Layer Applications." *Remote Sensing of*

1612 *Environment* 120 (May 2012): 70 - 83. <https://doi.org/10.1016/j.rse.2011.09.027>.

1613

1614 Voudouri, Kalliopi Artemis, Konstantinos Michailidis, Maria-Elissavet Koukouli, et al.

1615 "Investigating a Persistent Stratospheric Aerosol Layer Observed over Southern

1616 Europe during 2019." *Remote Sensing* 15, no. 22 (2023): 5394.

1617 <https://doi.org/10.3390/rs15225394>.

1618

1619 Warren, Stephen G., and Richard E. Brandt. "Optical Constants of Ice from the

1620 Ultraviolet to the Microwave: A Revised Compilation." *Journal of Geophysical*

1621 *Research: Atmospheres* 113, no. D14 (2008). <https://doi.org/10.1029/2007jd009744>.

1622

1623 Wei, Lesi, Huazhe Shang, Jian Xu, et al. "Cloud Top Pressure Retrieval Using

1624 Polarized and Oxygen A-Band Measurements from GF5 and PARASOL Satellites."

1625 *Advances in Atmospheric Sciences* 41, no. 4 (2024): 680 - 700.

1626 <https://doi.org/10.1007/s00376-023-2382-5>.

1627

1628 Zheng, Guangjie, Yang Wang, Allison C. Aiken, et al. "Marine Boundary Layer

1629 Aerosol in the Eastern North Atlantic: Seasonal Variations and Key Controlling

1630 Processes." *Atmospheric Chemistry and Physics* 18, no. 23 (2018): 17615 - 17635.

1631 <https://doi.org/10.5194/acp-18-17615-2018>.

1632

1633 Zhou, Yongbo, Xuejin Sun, Tero Mielonen, et al. "Cirrus Cloud Optical Thickness and

1634 Effective Diameter Retrieved by MODIS: Impacts of Single Habit Assumption, 3-d

1635 Radiative Effects, and Cloud Inhomogeneity." *Journal of Geophysical Research:*

1636 *Atmospheres* 123, no. 2 (2018): 1195 - 1210. <https://doi.org/10.1002/2017jd027232>.